UCLA
UCLA Electronic Theses and Dissertations

Title

Microfluidic Brain Slice Chambers and Flexible Microelectrode Arrays for in vitro Localized Stimulation and Spatial Mapping of Neural Activities

Permalink

https://escholarship.org/uc/item/91d7n7k0

Author

Tang, Yujie

Publication Date

2012

Peer reviewed|Thesis/dissertation

eScholarship.org Powered by the California Digital Library
University of California

UNIVERSITY OF CALIFORNIA

Los Angeles

Microfluidic Brain Slice Chambers and Flexible Microelectrode Arrays for *in vitro* Localized Stimulation and Spatial Mapping of Neural Activities

A dissertation submitted in partial satisfaction of the requirements for the degree Doctor of Philosophy in Mechanical Engineering

by

Yujie Tang

2012

© Copyright by

Yujie Tang

2012

ABSTRACT OF THE DISSERTATION

Microfluidic Brain Slice Chambers and Flexible Microelectrode Arrays

for in vitro Localized Stimulation and Spatial Mapping of Neural Activities

by

Yujie Tang

Doctor of Philosophy in Mechanical Engineering

University of California, Los Angeles, 2012

Professor Yongho Ju, Chair

In vitro neurobiological experiments using brain slices have played a key role in improving our understanding of the central nervous system. Microfabricated brain slice chambers and flexible semi-transparent multi-electrode arrays allow controlled local changes in the chemical environments as well as high resolution electrophysiology and optical recording of brain slices which would in turn provide further information of the complex neuronal system. In this study, we exploit the advantages of microfabricated devices, including a microfluidic brain slice chamber for localized chemical stimulation and a flexible microelectrode array for spatial mapping of neuronal activities, to investigate various biophysical properties of cortical spreading depression.

First, a microfluidic brain slice chamber is designed and fabricated to permit localized chemical stimulation to specific brain slice cortical regions. We build a numerical finite element model to predict the injected plume shape and the resulting ion distributions in the stimulated brain slice. Various characterization methods, including particle tracking velocimetry, fluorescent imaging and tissue staining, are implemented to verify the fluid dynamics predicted by our model. With the ability to fine control the stimulation area, we vary the stimulation size as well as the extracellular potassium concentration ($[K^+]_e$) to study the conditions for the onset of cortical spreading depression. We find a strong correlation between the threshold concentration and the slice area exposed to the increased $[K^+]_e$. Our results show that CSD is inducible under the conditions expected in migraine aura.

We then explore the use of a flexible microelectrode array to map spatiotemporal electrophysiological activities induced by localized chemical stimulation. We concurrently use the microfluidic device to initiate CSD in mice cortex and the electrode array to record electrical activities accompanying the spreading wave. Besides the consistency between optical and electrical recording, we observe the electrical responses similar to cortical spreading convulsion with a corresponding optical characteristic.

In summary, the microfluidic brain slice chamber has been demonstrated with a localized stimulation capability and used to probe the cortical spreading depression initiation and propagation properties. The concurrent use of the microfluidic and microelectrode array techniques has been demonstrated and is shown to be promising in addressing scientific questions. Our work demonstrates a successful implementation of novel microfabricated tools for the neuroscience research.

The dissertation of Yujie Tang is approved.

Chang-Jin Kim

Chih-Ming Ho

Kevin Christopher Brennan

Yongho Ju, Committee Chair

University of California, Los Angeles

2012

TABLE OF CONTENTS

LIST OF FIGURES

ACKNOWLEDGMENTS

Without my friends, colleagues, and mentors in graduate school, I would never have seen this work to its end. I want to give my profound thanks to all of those who have given financial, technical, intellectual, and emotional support during my years at UCLA.

To my committee: Chang-Jin "CJ" Kim, Chih-Ming Ho, K. C. Brennan and Y. Sungtaek Ju

To the members of Professor Ju's group: Katie Bulgrin, Gilhwan Cha, Jichul Kim, Youngsuk Nam, Stephen Sharratt, Yanbing Jia, Cheng Peng, Jinda Zhuang and Yangsu Na

To the Brennan Lab, both Bruins and Utes: Josh Chang, Katjusha Jushkina, Hector Lopez-Valdez, Jeremy Theriot, Jorge Mendez, Volodymyr bogdanov, Jay Vargas, Dan Kaufmann and Punam Sawant

To professors and colleaguess: Larry Hoffman, Andrew Charles, Dejan Markovic, Vaibhav karkare and Minji Zhu

To my family and friends

Thank You.

VITA

2003-2007	B.S., Microelectronics School of Electrical Engineering and Computer Science, Peking University, Beijing, China
2007-2012	Graduate Student Researcher/Teaching Assistant Mechanical and Aerospace Engineering Department University of California, Los Angeles, California

PUBLICATIONS

Tang YT, Kim J, López-Valdés HE, Brennan KC, Ju YS, Minimum Conditions for the Induction of Cortical Spreading Depression, in preparation

Tang YT, Kim J, López-Valdés HE, Brennan KC, Ju YS, Development and characterization of a microfluidic chamber incorporating fluid ports with active suction for localized chemical stimulation of brain slices. Lab on a chip 11(13):2247–54.

Tang YT, Kim J, López-Valdés HE, Brennan KC, Ju YS, Minimum Conditions for the Induction of Cortical Spreading Depression, the 54th American headache Society, June 21-24, 2012, Los Angeles, CA, USA.

Bogdanov VB, **Tang YT**, Multon S, Mamilov SA, Misyura AG, Schoenen J, Ju YS, Brennan KC, Preferential susceptibility and propagation of spreading depression in superficial cortical layers, the 54th American headache Society, June 21-24, 2012, Los Angeles, CA, USA.

Brennan KC, **Tang YT** , López-Valdés HE and Ju YS, Minimum Conditions for the Induction of Cortical Spreading Depression: Implications for Migraine with Aura, the 64th American Academy of Neurology Annual meeting, April 21-28, 2012, New Orleans, LA,

USA. Top 5 % of the program and, is highlighted in the "Scientific Program Highlights Plenary Session".

Sharratt S, **Tang YT**, Peng C, Cha G, Ju YS, Thermal Management of LED Lighting Systems using Low-Temperature Synthesized Cu Wicks on PCB Substrates, ASME 2011 International Mechanical Engineering Congress & Exposition, November 11-17, 2011, Denver, CO, USA

Tang YT, López-Valdés HE, Brennan KC, Ju YS, localized Induction of Cortical Spreading Depression Waves in Brain Slices Using Microfluidic Injection, MicroTas 2011, October 2-6, 2011, Seattle, WA, USA.

Tang YT, López-Valdés HE, Brennan KC, Ju YS, Microfluidic Brain Slice Chamber with Localized Injection Ports and Its Application to the Study of Cortical Spreading Depression, the 12th Annual UC systemwide bioengineering symposium, June 13-15, 2011, Santa Barbara, CA, USA.

Tang YT, Kim J, López-Valdés HE, Brennan KC, Ju YS, Microfluidic Chamber with Active Suction Ports for Localized Chemical Stimulation of Brain Slices, Oral presentation, MEMS 2010, January 24-28, Hong Kong, China.

CHAPTER 1

Introduction

In the field of neuroscience, neuronal function is investigated with different approaches. The most direct approach is *in vivo* study, where the circulation system is fully responsible for the nutrients supply to the brain. Preserving the conditions in a normally behaving animal, *in vivo* methods are considered a well suited model for observing the whole effect of a procedure on the animal. Yet, the extraordinary complexity of living organism offers abundant information that sometimes impedes the exploration of basic biological functions. The extreme opposite to the intact brain is the cell. The incubation solution of cells could be changed to directly study the cellular response. Organotypic brain slices share some characteristics with a single layer of cells. Moreover, as they continue to grow into a cellular network, they provide more network information than single cells. Acute brain slices which are cut directly from viable animals and used within 10 hours after the dissection preserve intact local neuronal anatomy and connection. Although losing the neurovasculature, these slices still contains similar neuronal connection and therefore are powerful tools to study the single channel ,synaptic, cellular and network functions (Dingledine et al. 1980; Lossi et al. 2009). They offer a simpler model to study the brain that is sometimes desirable.

As the brain slice preparation intends to mimic the *in vivo* brain, the approach serves as a preceding trial to investigate possible outcomes in potential *in vivo* experiments. The brain slice preparation is advantageous over *in vivo* preparation in the follow aspects: (1) After the

dissection, the fresh brain is sliced into about 400 μm thick slices. As several slices could be harvested from a single brain, different drug responses in a single animal could be investigated in parallel which improves both accuracy and efficiency. (2) Brain slices could be cut in desired anatomical planes so that regions that are difficult to reach in *in vivo* preparations are readily accessible(Khan et al. 2007). (3) Different depths are exposed on the surface of the brain slice at the same time offering opportunity to examine the depth/regional anisotropy of the brain.

Various tools have been developed to improve the spatial-temporal resolution in stimulating and recording the nervous systems. These tools are revisited and improved with the development of microfabrication techniques. Taking advantage of the design principles, microfabricated devices serve to improve the accuracy in detection and stimulation, provide user-friendly enclosed systems with integrated functionalities, and offer novel opportunities to study the neurological activities that cannot be realized by traditional approaches.

As the brain slice model proves to be a valuable tool, neuroscientists have refined ways to maintain the brain slice without its endogenous circulation systems since its first development. In a typical brain slice experiment, the slice is perfused by hyperoxygenated artificial spinal fluid (ACSF) continuously, which intends to force fresh supply of nutrients and oxygen to penetrate into the thickness of the slice and maintain a condition that best mimics the *in vivo* preparations. The unwanted gradient of supplied solution and gas concentration, however, inevitably exists throughout the thickness of the slice and is especially severe for thick brain slices (> ~500 μm). The center of the tissue having insufficient supply of nutrients and oxygen to

meet its metabolic requirement cause the whole slice to deviate from its physiological conditions. To improve the healthiness of a brain slice, a dense mesh underlying the slice is usually utilized to provide capillary based perfusion at the bottom side of the slice. Microfabricated post arrays have been proposed to provide better perfusion underneath the slice. These posts are integrated with the chamber, offering minimal contact with slice thereby maximize the contact area of the slice to the perfusion solution. Faster flow speed is realized thanks to the larger empty space in between posts. To improve the nutrients uptake, dual sided perfusion chambers have been designed so that the top side of the slice is perfused with high speed solution as well (Blake et al. 2007). Forced convection is used to enhance perfusion rate by increasing the interstitial flow through the slice (Rambani et al. 2009; Hill and Greenfield 2011). Needles inserting into the slices allow nutrients directly reach the region that is lack of nutrient supply (Choi et al. 2007).

Secondly, it's always desirable to control the spatial extent of the chemical applied to the brain slices. The brain is organized in different functional modules. To understand different responses, it is of great interest to target stimulation at specific locations. Besides, spatially restricted drug application offers opportunities to study volume-dependent neuronal activities. Traditional ways to apply chemical stimulation to the brain slice includes switching the whole perfusion solution to stimulation drugs or using a pulled glass micropipette to locally apply the drug (Ling and Gerard 1949). Changing the bath perfusion until the drug takes effect takes time. Also the whole slice is influenced. To improvement the spatial-temporal resolution in stimulation, glass pipettes have been used to apply a laminar stream of drug so only a stripe of the brain slice is stimulated. To increase the spatial resolution, coaxial (Feinerman and Moses 2003)and double barreled glass micropipette(Davis and Gore 1987) are used where injection and

aspiration are applied simultaneously to confine the plume. Microfabrication techniques make the fabrication of the complicated pipettes easier and with a better repeatability. Microchannels are designed to confine the lateral extent of the laminar flow which perfuses a stripe of the brain slice in the downstream of its inlet (Blake et al. 2007). Small openings in the bottom of the chamber that have delivery channel connected allow local slow fusing of drugs into the slices(Heuschkel et al. 1998; Mohammed et al. 2008). Microfabricated pipettes are implemented to applied chemicals to brain slices and protein arrays, with a reduced opening size(Christ and Turner 2011; Kaigala et al. 2011; Ainla et al. 2012). The underlying micro-perfusion systems permit successful integration of various ports in one device without blocking the top space for imaging.

Modern microscopy plays an important role in studying neurobiology. In most cases, microfabricated brain slice chamber are compatible with a majority of microscopy techniques in either upright or bottom up form. Besides the optical approach, an alternative is to study the electrophysiology of the brain. Pulled glass micropipettes have been used for recording electrical signals of the nervous system for a long time. Number of recording sites is limited by practical issues. Microfabricated multi-electrode array has overcome the traditional imitation in electrodes amount and have thereby advanced our understanding of the brain to a great extent(Rutten 2002; Sarje and Thakor 2004; Cheung 2007). Conceptually, MEAs designed for recording and stimulating neuron networks in *in vivo* experiment can be readily transformed to be used for brain slices. In addition to the flat electrodes widely used on the brain surface, 3D/extruding electrodes play an important role in slice recordings. This is because the cutting induced damaged cells at slice surface increase the distance from the signal source to the electrode and as

a result, the electrode field strength detected is attenuated with a squared distance function. MEAs designed for brain slice study use flat or extruding electrodes to record a large amount of data simultaneously in the slice(Heuschkel et al. 2002; Rajaraman et al. 2007). MEA technology has been integrated into microfluidic slice chambers with extruded needle/tower shaped channels(Heuschkel et al. 1998; Rajaraman et al. 2007). A recent development of brain slice chamber incorporating microfluidic channels with Ag/AgCl wires in the channel for electrophysiology recording successfully combines the localized stimulation function with simultaneous electrical mapping in a extended area (Scott et al. 2012). MEAs that use polymers as the carrier and insulation material offer the unique advantage of mechanical flexibility. Being transparent as well, these flexible MEAs could be adapted in brain slice research as a valuable add-on to the microfluidic chamber.

This dissertation explores the opportunities of integrating microfluidic and microelectrode array techniques into brain slice study for localized chemical stimulation and 2D electrical characterization of the brain slices. We focused on the study of cortical spreading depression (CSD) using the apparatus developed. CSD is a neuronal phenomenon that's closely related to migraine aura, head trauma and stroke(Somjen 2001). It is also a spreading event in the brain cortex which initiates from a local source. The devices we developed are especially valuable for assessing CSD initiation and propagation characteristics. We demonstrate the ability to deliver chemicals in a localized manner to certain location of the brain cortex and investigate the volume dependency of CSD induction. We further investigate the minimum conditions for the initiation of CSD by varying the stimulation size. We then develop a flexible MEA for

recording electrical responses during CSD propagation and demonstrate the first 2D CSD recordings in a brain slice.

In Chapter 2, we describe the development of a microfluidic brain slice chamber. We use a combination of injection and suction ports to confine an injected plume. The device is fabricated using a two layer soft lithography technique. We demonstrate the fine control of injected liquid plume using the microfluidic device.

In Chapter 3, we characterize the quantitative behavior of the device used for stimulating brain slices. Particle tracking velocimetry is implemented to measure the velocity of injection and suction fluids. Fluorescence imaging based optical sectioning with a high numerical aperture lens is used to observe the 3D profile of a confined plume. Dyes penetrating into the slice reveal the 3D extent of the plume inside a slice. A multiphysics numerical model is built to illustrate how injected fluid behavior with and without the brain slice. Simulation results are consistent with experiment results for situations with and without brain slices. A demonstration of inducing CSD with the device is shown.

In Chapter 4, we investigate the minimum condition for CSD induction using the developed microfluidic device. We find a strong concentration-area relationship of the initiation condition for CSD. We further use two-photon laser scanning microscopy to measure the volume enclosed by the injected plume inside the slice. The measured results are again a good match with the predicted concentration profiles by our model.

In Chapter 5, we report the development of a polymer based flexible microelectrode array used to measure the slow potential change accompanying CSD. We develop the data analysis standard to characterize near DC signal using polarizable electrodes. Combing the microfluidic

localization stimulation, optical recording and electrical recording capability, we discover a possible scenario for cortical spreading convulsion.

CHAPTER 2

Development of a Microfluidic Chamber Incorporating Fluid Ports with Active Suction for Localized Chemical Stimulation of Brain Slices

We report a novel microfluidic chamber incorporating fluid ports with active suction to achieve localized chemical stimulation of brain slices. A two-level soft-lithography process is used to fabricate fluid ports with integrated injection and suction holes that are connected to underlying microchannels.

2.1 Background

In vitro neurobiological experiments using brain slices have played a key role in improving our understanding of the central nervous system. Unlike cell cultures, brain slices retain local neuronal connections and anatomy(Snow et al. 1983), closely approximating intact brains. Furthermore, vascular and metabolic influences that exist in *in vivo* preparations are effectively suppressed(Croning and Haddad 1998), enabling independent tests of biological hypotheses involving neurovascular coupling.

The brain is organized into different functional modules(Edelman and Mountcastle 1982). The ability to induce or suppress neuronal activity in specific modules through localized delivery is of great interest to neuroscientists. This is especially true for spatio-temporally varying neural

phenomena such as seizures and cortical spreading depression (CSD), which initiate and spread from a specific focus. Delivery of a chemical agent stimulating or suppressing such phenomena should be precisely confined within a particular area while the surrounding neurons get information only through the neuronal network.

Glass micropipettes have long been used to inject soluble chemicals into extracellular or intracellular spaces of brain tissues and study their impacts(Ling and Gerard 1949; Myers 1967; Kottegoda et al. 2002). Microfluidic devices have recently emerged as an elegant alternative platform to inject chemicals into extracellular spaces of brain slices. They are less invasive, offer potentially higher spatial resolution, and can be integrated with wide ranges of stimulation and sensing modalities.

Several research groups have developed microfluidic devices for cell cultures with localized stimulation capability (Arai et al. 2001; Blau and Ziegler 2001; Yang et al. 2002; Peterman 2003; Peterman et al. 2004; Hung et al. 2005; Pearce et al. 2005; Millet et al. 2007). These devices, however, are not suited for tissue slices that require a continuous supply of nutrients and oxygen. Tissue slices also have finite thicknesses and healthy cells tend to be located away from the exposed surfaces.

Microfabricated probes(Lovchik et al. 2009; Shiku et al. 2009; Ainla et al. 2010; Queval et al. 2010) have been developed to mimic conventional concentric dual glass micropipettes to locally release chemicals on biological samples. Queval *et al*.(Queval et al. 2010) applied such microfluidic probes for localized chemical injection into artificially-thinned cultured brain slices for bottom-up imaging using an inverted microscope.

Microfluidic probes, however, have limitations especially when applied to brain slices. These relatively large probes positioned above the slices block optical views and also impede the placements of electrodes and other transducers directly above regions that are chemically stimulated.

Planar microfluidic platforms placed underneath a brain slice can circumvent these difficulties and allow much greater flexibility in designing the geometry of ports and their relative arrangements. Planar devices can also be readily scaled up to incorporate injection ports on multiple discrete locations. Moreover, they allow for visualization, spectroscopic recording, and electrode placement from above the slice, avoiding modification of most commonly used slice physiology setups.

Several studies have shown that planar microfluidic devices can induce controlled changes in the chemical environments of brain slices(Neeves et al. 2006; Blake et al. 2007; Choi et al. 2007; Cullen et al. 2007; Mohammed et al. 2008). Blake *et al*. (Blake et al. 2007)developed a three-layer slice chamber with multiple inlets. The chamber delivers chemicals along a line path as part of an overall perfusion flow. A focal delivery of chemicals was therefore not feasible. Mohammed *et al*.(Mohammed et al. 2008) incorporated a microfluidic port on the bottom surface of a perfusion chamber to locally inject chemicals into a slice pressed against the chamber surface. Other studies reported three-dimensional microdevices with penetrating micro-ports to deliver oxygen, nutrients, and possibly neuromodulators into thick brain slices(Choi et al. 2007). However, the impact of mechanical trauma and tissue damage must be assessed for each neurological phenomenon of interest.

A key challenge for planar microfluidic devices has been the difficulty in sealing slice-port interfaces for localized delivery of chemicals. Simply pressing a slice against fluidic ports is problematic as it may generate undesired mechanical stimulation or possibly damage the brain tissue. This motivates alternative designs to achieve localized chemical stimulation while circumventing deleterious effects associated with physical sealing.

In the present work, we report our progress in developing a microfluidic chamber where we employ active fluid suction, as opposed to physical sealing, to achieve localized injection of chemicals. We fabricate the chamber using a two-level soft-lithography process and perform flow and concentration visualization experiments to demonstrate effective confinement of injected chemicals. A successful localized induction of cortical spreading depression is then demonstrated by focal delivery of a potassium chloride solution.

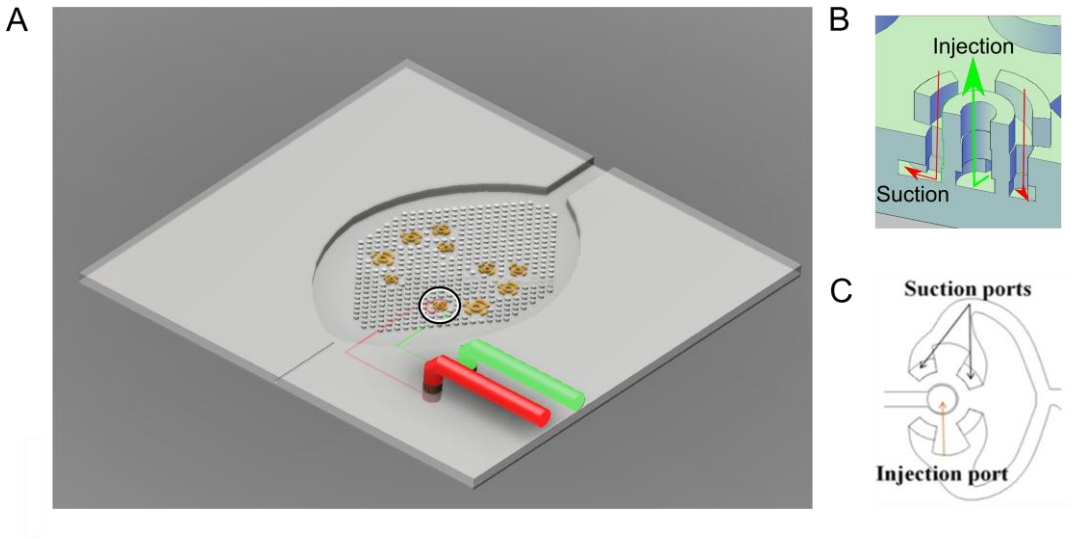

Figure 2.1: Design of device.

(A) Schematics of the perfusion chamber incorporating integrated fluid injection/suction ports for localized chemical stimulation of brain slices. The cut view (B) and top view (C) of the fluid port (black circle in (A)) with one injection hole surrounded by four suction holes

2.2 Chamber Design

The design of our microfluidic chamber is schematically illustrated in Fig. 2.1. The chamber incorporates a base layer containing an array of microposts over which a brain slice is placed. As demonstrated in a previous study(Passeraub et al. 2003), a dense post array is effective in ensuring a laminar flow of an oxygenated artificial cerebrospinal fluid (ACSF) and hence maintaining slice viability. The array also mechanically supports the brain slice while

minimizing mechanical trauma. In our design, the post array is denser near the side walls of the chamber to prevent the formation of recirculating flow patterns.

Select microposts are replaced with fluid ports, each consisting of a single injection hole surrounded by multiple suction holes. The suction holes actively confine an injected fluid and thereby eliminate the need for physical sealing. The port locations are selected to approximately follow the shape of the neocortical layer of mouse brain slices. The diameter of the injection holes is approximately 100 μm, comparable to the sizes of typical functional modules of rodent brains(Purves et al. 1992).

2.3 Device fabrication

The microfluidic chamber is made of PDMS (polydimethylsiloxane) and fabricated using a soft lithography technique(Xia and Whitesides 1998). A set of two molds is made by patterning negative photoresist layers. The first mold is for fabricating the underlying supply and suction channels and the other for the post arrays, fluid ports, and through holes.

Fig. 2.2 illustrates the cross-sectional views of a fluid port after each major processing step. A thin layer of negative photoresist (SU-8 2007, MicroChem Inc.) is first spin coated at 3000 rpm to a thickness of appropriately 10 μm on a clean dehydrated wafer to enhance the adhesion of a subsequent photoresist layer. For the first mold, a second layer of SU-8 (SU-8 2100, MicroChem Inc.) is next spin coated at 3300 rpm to a thickness of approximately 100 μm and soft baked at 95°C on a levelled hot plate for 25 minutes. The hot plate temperature is ramped gradually from 65°C to 95°C over approximately five minutes to reduce thermal

stress. The wafer is cooled down to room temperature before the next process step. The photoresist layer undergoes exposure, post exposure bake (PEB), development, and hard bake according to the supplier's recipe as illustrated in Fig. 2.2A.

For the second mold, a two-level structure is fabricated using a procedure illustrated in Fig. 2.2B. Alignment marks are first created in a PECVD (plasma enhanced chemical vapour deposition) silicon nitride layer using RIE (reactive ion etching). A 100 µm-thick SU-8 layer is then spin coated, soft baked, UV exposed, and baked again. This base layer is used to define the post array and the bottom surface of the perfusion chamber. A second 100 µm-thick SU-8 layer is next spin-coated and subjected to soft bake, UV exposure, and post exposure bake steps. This second SU-8 layer defines the suction holes and the through holes that will connect the injection holes to the underlying microchannels. The two resist layers are developed and rinsed in isopropanol and water before they are hard baked at 150°C. The double layer SU-8 mold fabrication results are shown in Fig. 2.3A. With the aid of alignment marks, the first and second layer of SU-8 are well aligned. Uniformity of the top post height is excellent. This ensures that when PDMS is cured on the mold in the following steps, through holes can be successfully fabricated when a cover is tightly attached to the top of these posts. Microcracks formed after development disappear after curing at 150^{o}C for 5 minutes.

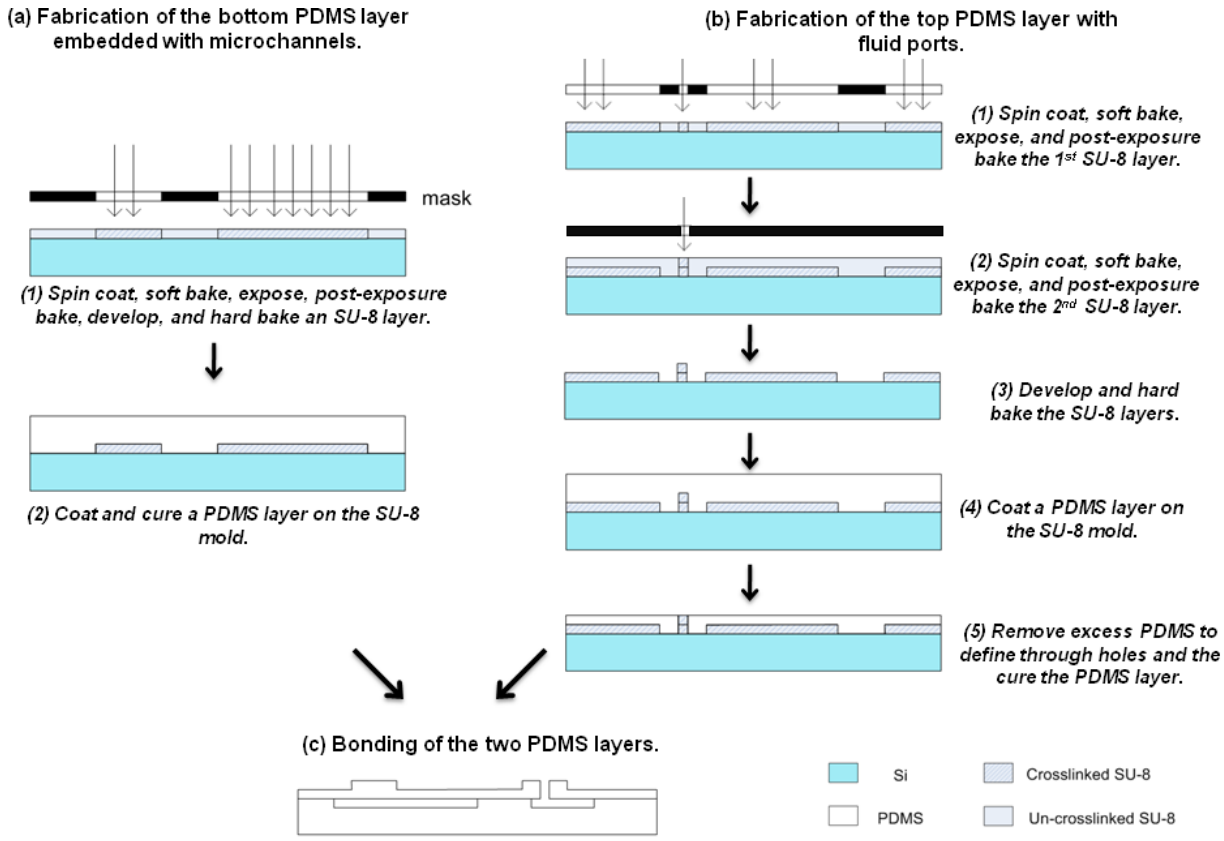

Figure 2.2: Abbreviated process flow for fabricating the dual-layer PDMS brain slice chamber.

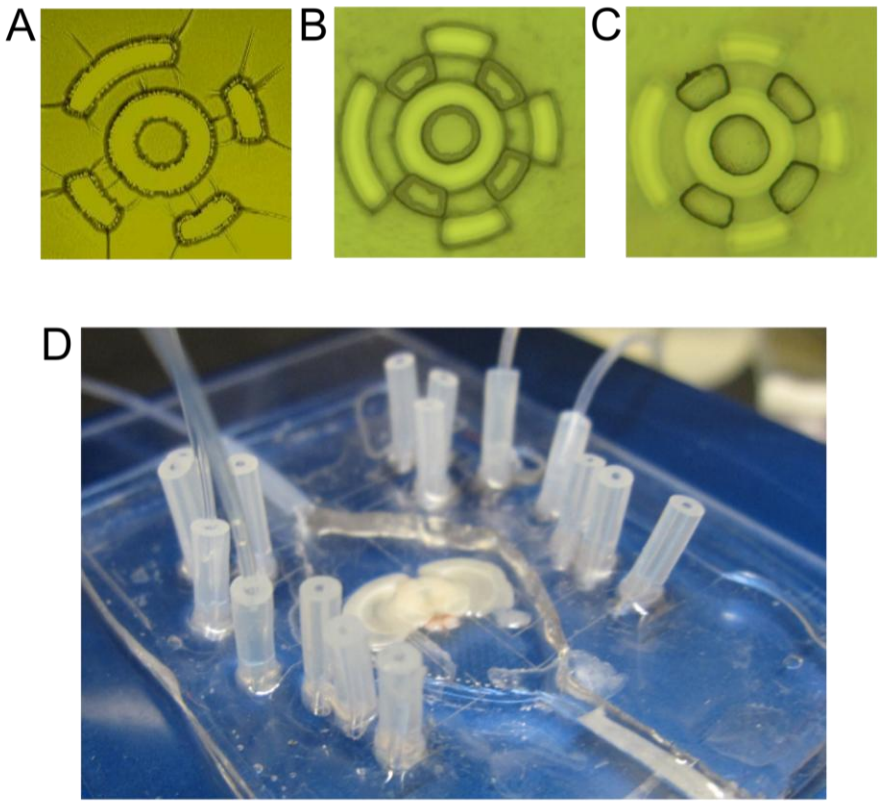

Figure 2.3: Microfabrication results.

(A) First layer SU-8 mold during step 3 in Fig 2.2B in the absence of hard baking. Cracks are visible. (B) Double layer SU-8 mold. Micro-cracks disappeared after hard baking. (C) Uniform top layer height is demonstrated by focusing on the mold top. (D) Bonded PDMS brain slice chamber. In the center of the chamber a brain slice is shown.

We prime the photoresist mold in HMDS (hexamethyldisilazane) vapour overnight to facilitate the peeling process. A 10:1 mixture of PDMS base and curing agents (Sylgard 184; Dow Corning) is degassed and poured onto each of the two molds. The molds are placed in a vacuum chamber for 10 minutes until all the air bubbles trapped between the PDMS and SU-

8 layers are released. A sheet of polyethylene is then placed against the PDMS layer to squeeze out any residual PDMS and open the through holes. A weight is put on the polyethylene sheet to ensure tight contact. The PDMS layers are cured on a hot plate at 75 ºC for two hours. To illiminate the shrinkage effect of PDMS during curing, channel and hole PDMS membranes are cured on a same hot plate for same duration.

The two PDMS layers are peeled off from their molds and placed in contact with each other after an oxygen plasma treatment (600mTorr, 70 W for 10 seconds). Methanol is used as a lubricant between the layers to facilitate alignment. After the alignment is complete, the assembly is heated on a hotplate to evaporate away any residual solvent. The assembly is then baked at 95 ºC overnight to achieve strong bonding between the PDMS layers. The final PDMS device is bonded to a custom-made PDMS slice chamber frame to complete the perfusion chamber (Fig. 2.3D).

2.4 Summary

We domonstrated a double layer PDMS chamber fabricated using soft lithography techniques. The device is compatible with existing brain slice physiology setups and can easily be implemented. The low-cost fabrication process allows users to design a fine-tuned device for their specific application. The chamber is designed with the capability to inject and remove liquid simultanously for forming a localized liquid plume.

CHAPTER 3 Characterization of a Microfluidic Chamber Incorporating Fluid Ports with Active Suction for Localized Chemical Stimulation of Brain Slices

Fluorescence imaging, particle tracking velocimetry, and cell staining are used to characterize flows around a fluid port with or without active suction to validate effective localization of injected chemicals. A numerical model based on finite element method is developed to predict the velocity fields and concentration distribution around the port and inside the slice. The model predicted results are consistent with observations in experiments for both conditions. Our results show that an essential condition for the success in locally stimulation of the brain lies in the properly adjusted injection/suction velocity ratio. To demonstrate biological applicability of the chamber, we show an induction of cortical spreading depression (CSD) waves in mouse brain slices through controlled focal delivery of potassium chloride solution. The present work provides a useful framework for device operation conditions upon which the localized stimulation function can be implemented.

3.1 Background

The characterization of the device performance is carried out before we conduct a systematic brain slice study. To ensure a predicted functionality of the device, the flow condition inside the chamber needs to be finely controlled. Fluid inside the microfluidic chamber is

described by the Navier-Stokes equations. When a second fluid is injected through the injection port, both advection and diffusion determines the distribution of the second substance inside the bulk solution. The Péclet number is used to describe the ratio of advection and diffusion effect and is defined as:

$$Pe = \frac{L\,U}{D} \tag{3.1}$$

where L is the characteristic length, U the velocity and D the mass diffusivity. In most microfluidic systems, the Pe number is much larger than 1 indicating that direct flow, rather than diffusion, has a dominant role on the mass distribution.

When the fluid enters the brain, the flow motion is significantly hindered by the densely packed neurons, glial cells and vasculature. The diffusion predominantly happens through the extracellular space of the brain tissue. Extensive experiments have shown that the movement of molecules in the extracellular space could be modeled as a diffusion process in a porous medium. The hindered diffusion process is characterized by an effective diffusion coefficient that represents the volume fraction and the tortuosity of the brain extracellular space.

The system to be characterized includes flow in free medium as well as in a brain slice. Therefore, a combined flow-diffusion model describes the spreading of substances from the injection port. We use finite element method to numerically predict the flow motion and particle distribution.

There are several ways to visualize the flow experimentally. Optical images taken with a high numerical aperture lens record quasi steady state cross sections of the 3D plume along its vertical axis. As the diffusion does not play an important role in the free medium, each scan has a

clear plume boundary. Particle tracking velocimetry is an effective way to measure the laminar flow velocity. It applies a sparse amount of particles into the flow and measures the displacement of the seeds assuming the movement of the seeds is identical to that of the flow.

In this chapter, we utilize optical sectioning, particle tracing and tissue staining approaches to characterize the flow motion caused by the total perfusion flow inside the chamber and local injection and suction activity around the port in the absence of a brain slice and with a brain slice. We compared the results to numerically predicted flow profiles and find the two agree with each other. Lastly, to demonstrate biological applicability of the chamber, we use a controlled focal perfusion of potassium chloride solution to induce cortical spreading depression waves in mouse brain slices.

3.2 Materials and Methods

3.2.1 Brain slice chamber characterization setup

The experimental setup we use to characterize our devices and perform CSD induction experiments is shown in Fig. 3.1. In order to maintain the viability of a brain slice, the assembled chamber incorporates an inlet and an outlet port to sustain continuous flows of an oxygenated artificial cerebrospinal fluid (ASCF) solution over and underneath the brain slice at 32±1ºC. This main ASCF solution is delivered to the chamber using gravity at 2 ml/min. A piece of filter paper (not shown) is placed at the outlet to minimize flow fluctuations. A platinum wire (300 μm in diameter) is placed on top of the slice, but away

from the gray matter area of interest, to immobilize the slice at the beginning of each experiment.

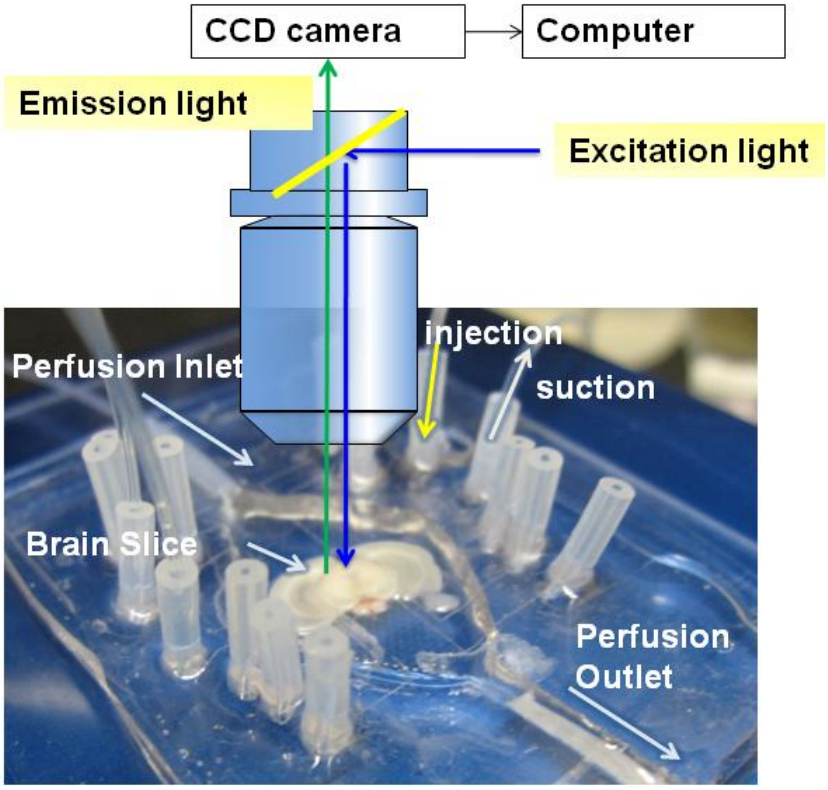

Figure 3.1: Experimental setup for the microfluidic chamber testing and brain slice experiments.

Multiple Tygon tubings (ID: 0.02" and 1/8") are bonded to the inlets and outlets of the microchannels. Two separate pumps are used for independent control of injection and suction, respectively. A syringe pump (sp1001 Pump; WPI, Sarasota, FL) is used to deliver a fluid into the injection port at mean velocities of the order of 0.001 m/s to 0.1 m/s. A

vacuum pump is used to create suction flows at mean velocities of the order of 0.01 m/s to 0.1m/s.

Our parametric simulation study indicates that the profile of a chemical plume is determined primarily by the ratio of injection to suction flow rates rather than their individual values under the present experimental conditions. At high flow rates, the flows may exert an appreciable shear stress on the brain slice surface. The lower limit to the injection flow rate was set primarily by the stability of a syringe pump in our study and can be reduced by using a pressure-driven pumping scheme in combination with a flow resistor. We do not observe any mechanically induced CSD events for all flow rates used in the present study. More systematic studies, however, may be necessary to rigorously elucidate the upper limit on the acceptable flow rates for different types of slice experiments.

The brain slice is imaged using a 4x objective lens (UPlanSApo, Olympus America, Melville NY) coupled either directly to a high sensitivity camera (Watec 902H2 Ultimate, Tsuruoka, Japan) via a tube lens (for optical intrinsic signal imaging) or through a filter cube (Chroma Technology) for epifluorescence imaging.

3.2.2 Slice preparation

Experimental protocols are approved by the UCLA Chancellor's Animal Research Committee. Female C57Bl/6 mice (25–30 g) are housed at 21°C on a 12-h light–dark cycle. Food and water are available without restriction. Deep anesthesia is achieved with isoflurane. The animal is decapitated and the brain is quickly removed and submerged in an ice-cold

oxygenated ACSF solution (ionic composition: 125 mM NaCl, 3 mM KCl, 1 mM $MgSO_4$, 2 mM $CaCl_2$, 1.25 mM NaH_2PO_4, 25mM $NaHCO_3$ and 10mM glucose) for 1 minute before being mounted on a slicer. Coronal slices of 400μm thickness are then cut in ice-cold oxygenated ACSF solution with a standard vibratome (MA752 Motorised Advance Vibroslice, Campden Instruments). The slices are then incubated in an oxygenated ACSF solution at 28°C for one hour before the experiments. For all the experiments, the slices are imaged within 1-3 hours after harvest.

3.2.3 Numerical simulations

3-D multi-physics finite element (FEM) simulations are performed to predict the flow and concentration profiles for different combinations of the injection and suction flow rates. We solve the Navier-Stokes equations for fluid dynamics and the time-dependent convection-diffusion equation for mass transport. Two sets of simulation are conducted: one without a slice (Fig. 3.3 and Fig. 3.4) and the other with a brain slice placed on the port (Fig. 3.5). A finite gap of approximately 25 μm between the bottom surface of the brain slice and the top of the fluidic port is assumed. A parametric study indicates that the predicted concentration profiles do not depend sensitively on this gap.

The density and viscosity of ACSF are assumed to be those of water. The mass diffusivity of fluorescein molecules in ACSF is assumed to be comparable to that in water ($2x10^{-9}$ m^2/s). A parametric study suggests that mass diffusion in ACSF is not significant since the Peclet number is much greater than 1 for all cases considered in the present work.

The effective diffusivity within brain slices is set to be $0.2x10^{-9}$ m^2/s based on previous experimental results(Nicholson and Phillips 1981; Nicholson and Tao 1993).

3.2.4 Optical Sectioning

A small amount of fluorescein (< 0.1%) is added to a solution of ACSF and the mixture is injected through the injection hole. A high numerical aperture lens (20x, NA = 0.95 Olympus, XLUMPlanFI) is used to obtain 2D slices of fluorescence intensity profiles in the depth (z) direction. We first set the lens focus at the bottom surface of the chamber. We then raise the lens incrementally using a micro-stepper while recording images at each z-location. A discrete composite 3-D concentration profile of the fluorescein plume can be reconstructed from the recorded 2D images.

3.2.5 Particle tracking velocimetry

We further use 2-D particle tracking velocimetry (PTV) to characterize the velocity field around the port. Seed microspheres (polystyrene bead, 1μm, Polysciences, Inc) are pre-dispersed in an ACSF solution introduced into the injection port. The locations of these seed particles are tracked using a high speed video camera (Fastcam MC2, Photron) operating at 10000 frames/s. By analyzing the particle trajectories, one can construct the velocity fields around the fluid port.

We discuss the concentration (Fig. 3.3 and Fig. 3.5) and velocity profiles obtained

from the numerical simulations and compare them with our experimental results in the next section.

3.3 Result and Discussion

3.3.1 Demonstration of the confinement of injected chemicals through active suction

Fig. 3.2 shows fluorescence images we obtain while injecting an ACSF solution mixed with a fluorescent dye (fluorescein isothiocyanate; FITC; Sigma-Aldrich Inc.) into the port without (a,c) or with (b,d) active suction. In the absence of active suction, the injected fluorescent dye is convected downstream by the main perfusion flow, forming a broad lateral plume. Since the Peclet number is much greater than 1, the effect of mass diffusion is small. With a sufficiently strong suction, the fluorescence dye is effectively confined and no "leakage" of the fluorescence dye downstream of the port is observed.

Images 3.2(c) and 3.2(d) are obtained with a brain slice placed on top of the port whereas images 3.2(a) and 3.2(b) are obtained without a brain slice. Since the slice has a finite optical thickness and scatters light, the images of the fluorescent plumes are more blurred in images 3.2(c) and 3.2(d) compared with images 3.2 (a) and 3.2 (b). However, the images do suggest that the active suction is effective in confining injected chemicals in actual brain slice experiments.

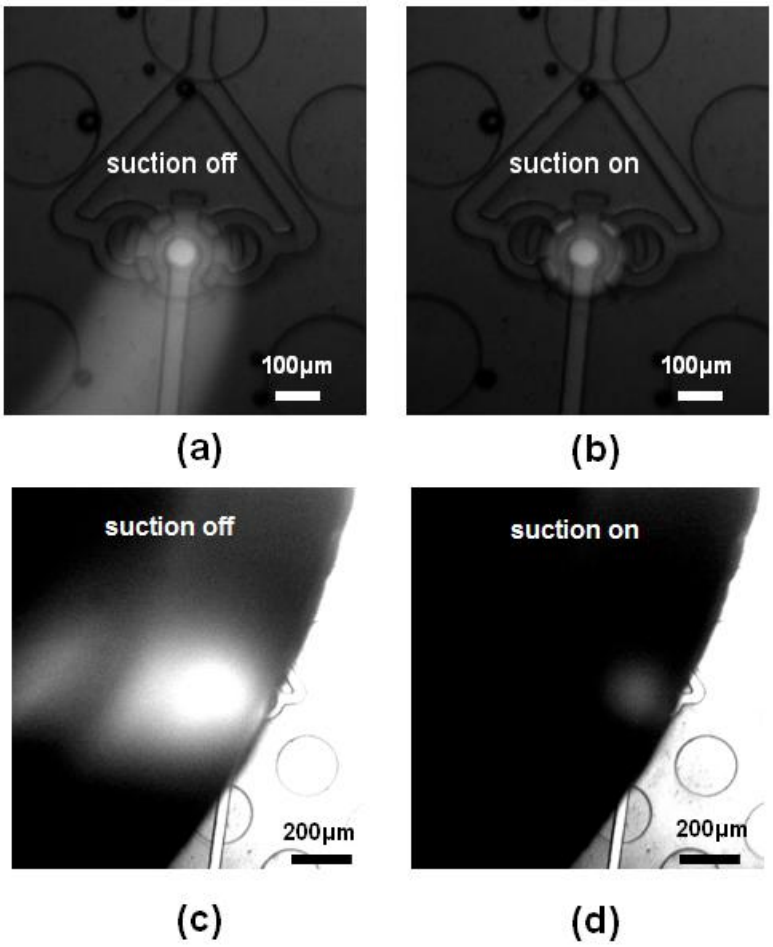

Figure 3.2: Fluorescence images of the injected flows: (a, b) without a slice and (c, d) with a brain slice placed on the port.

3.3.2 Concentration/velocity profile characterization

To further quantify the relevant characteristics of the device, we first use fluorescence microscopy to determine spatial concentration profiles of an injected chemical under different combinations of injection and suction rates. We perform these experiments in the

absence of a brain slice to avoid complications associated with absorption and scattering of light within the brain slice.

We examine three different combinations of injection and suction rates: Case 1 (suction dominant), Case 2 (suction comparable to injection), and Case 3 (injection dominant). The predicted concentration profiles across a port cross section are shown as colormaps in Fig. 3.3a. Fig. 3.3b shows top views of the measured fluorescence intensity profiles at a plane right above the fluidic port. The mean injection and suction velocities for each case are: 0.025 and 0.099 m/s (Case 1); 0.080 and 0.014 m/s (Case 2); 0.080 and 0.099 m/s (Case 3).

For Case 1 (suction dominant), the injected chemical forms a vertical plume that is confined below the top surface of the port. Under this condition, the injected chemical does not reach the brain slice. In the opposite condition, i.e. Case 3 (injection dominant), the injected chemical leaks out of the port forming a long lateral plume that merges with the main perfusion flow (directed perpendicular to the page). At optimal flow rate ratios (Case 2), the plume still exceeds the top surface of the port but is confined laterally and does not merge with the main perfusion flow. This is the condition we use in our later localized CSD stimulation experiments.

The experimentally determined plume boundary, defined as the locations of maximum slope in each fluorescence intensity profile, is marked with black symbols on the simulation results in Fig. 3.3a. The experimental plume profiles agree well with the simulation results for all three cases.

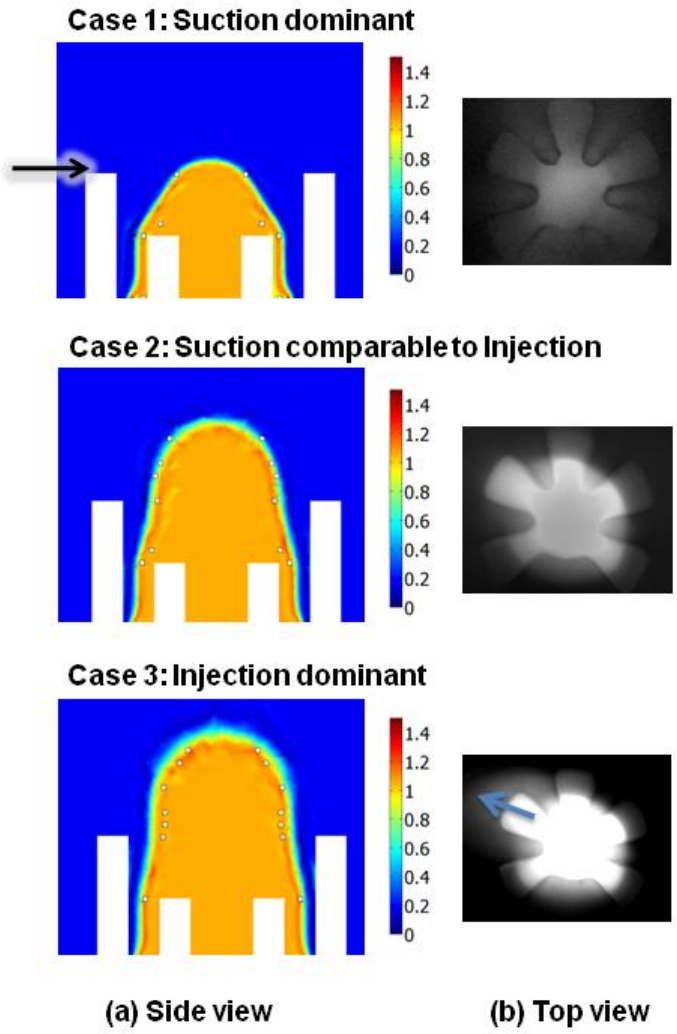

Figure 3.3: Concentration profiles around the injection ports.

(a) Side view: the experimentally measured profiles (black symbols) compare well with the simulation results. The profiles are taken on cross-sectional planes perpendicular to the main perfusion direction (the black arrow shows the horizontal location). (b) Top view: fluorescence images taken at the plane right above the port (black arrow in (a)). The blue arrow indicates the direction of the main perfusion flow.

The predicted velocity profiles are also consistent with the PTV results. Fig. 3.4 shows the top views of the port at two different *z*-levels (distance from the bottom chamber wall) with predicted velocity vectors shown in black arrows and measured velocity vectors in green arrows. For Case 3, the seed particles are mostly directed into the suction holes at a lower *z*-level (just above the top surface of the post). At a higher *z*-level, the particles follow the main perfusion flow rather than being directed into the suction holes, indicating unsuccessful confinement. When suction is comparable to injection (Case 2), leakage of the injected fluid is eliminated and the injected particles are directed to the suction holes even at the higher z-level. Under this condition, the plume is successfully localized around the port.

3.3.3 Cell staining experiments

Fluorescent microscopy is complemented by cell staining experiments to further demonstrate localized chemical injection in the presence of a brain slice. Fig. 3.5c shows the fluorescence images obtained from the top of brain slices for five different injection flow rates. The mean injection velocity increases from the left to the right images (V_{i} = 0.0043; V_{ii} = 0.0210; V_{iii} = 0.0275; V_{iv} = 0.0325; V_{v} = 0.0415 m/s). The mean suction velocity is fixed at 0.0180 m/s. The right most image corresponds to a situation where the plume just starts to lose its confinement.

The fluorescence images do demonstrate systematic increases in the chemical plume size with increasing injection flow rates. Due to scattering of light across the thickness of a slice, however, it is not a trivial task to directly correlate a fluorescent intensity profile with

the plume size.

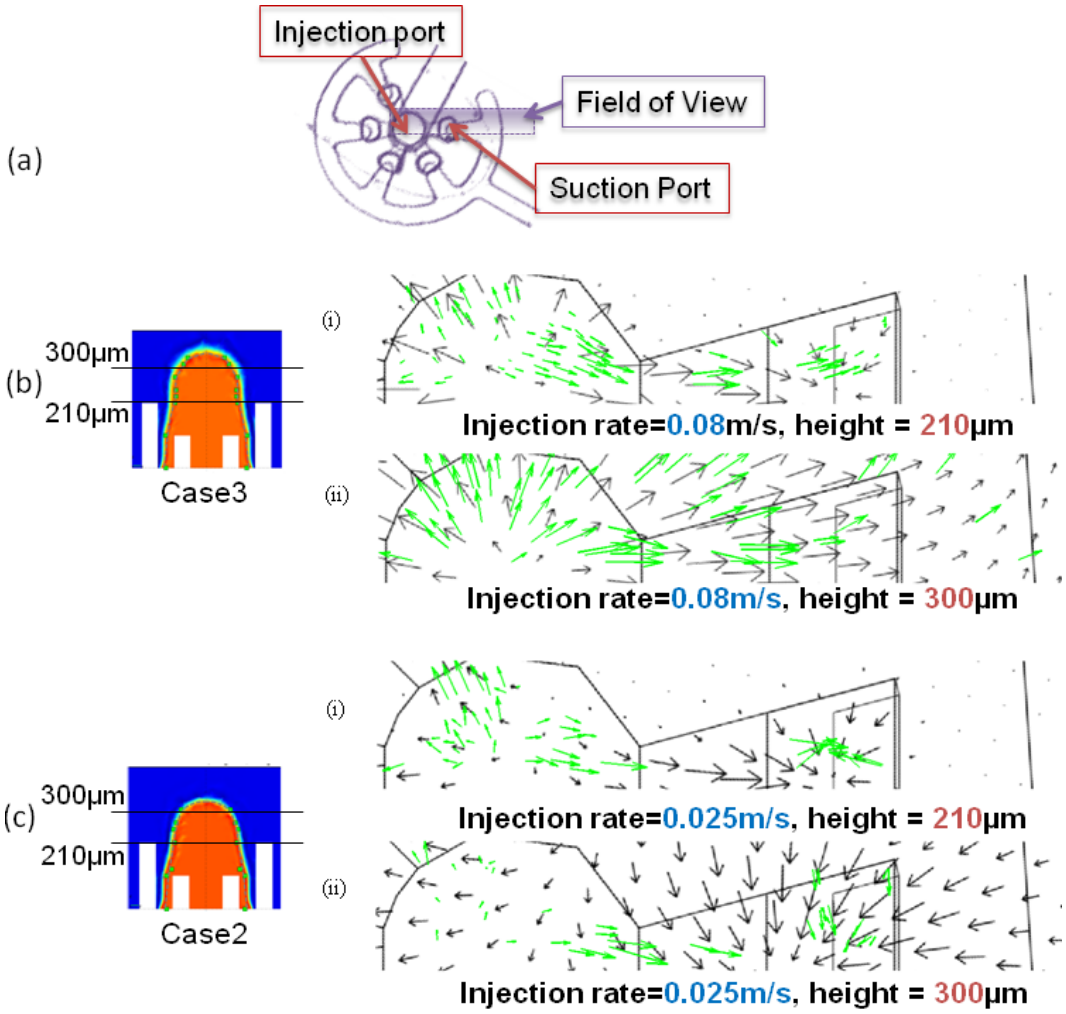

Figure 3.4: Particle tracking velocimetry results.

(a) Field of view (the rectangular area). (b-c) Predicted (gray arrows) and experimentally obtained (green arrows) velocity fields for (b) Case 3 (Injection dominant) and for (c) Case 2 (Injection comparable to suction) at two different z-levels.

To circumvent this difficulty, we inject an ACSF solution containing a cell-staining dye for a short period (30sec) and examine the spatial extent of cell staining. We perform two different sets of experiments using two different dyes: trypan blue (Sigma-Aldrich) and methylene blue (0.25% in potassium PBS, Sigma-Aldrich).

Trypan blue does not stain intact live cells but only cells with damaged membranes(Freshney 2005). The bottom layers of brain slices mostly contain such dead or otherwise damaged cells due to trauma experienced during slicing. Trypan blue staining experiments therefore allow us to gauge the spatial extent of a chemical plume in contact with the brain slice bottom surface.

Methylene blue, in contrast, stains intracellular structures (rough endoplasmic reticulum) of live cells(Bancroft and Gamble 2008) and allows us to locate healthy cells *within* the brain slice that come in contact with the injected chemical.

Fig. 3.5a shows the predicted concentration profiles at the bottom surface of the brain slice for the five different injection flow rates. The images of cells stained with trypan blue (discrete dots) are superposed on the numerical simulation results. The spatial distributions of the stains are consistent with the simulation results, exhibiting systematic increase in the areas populated by the stained cells with increasing injection-to-suction flow rates. Most stained cells are located within regions with predicted relative concentrations > 0.7. The present numerical model does not account for up-take of the dye molecules by cells. We note in passing that the stain imaging is performed after turning the slices over and, during this extra handling process, some of surface dead cell layers were lost due to mechanical abrasion.

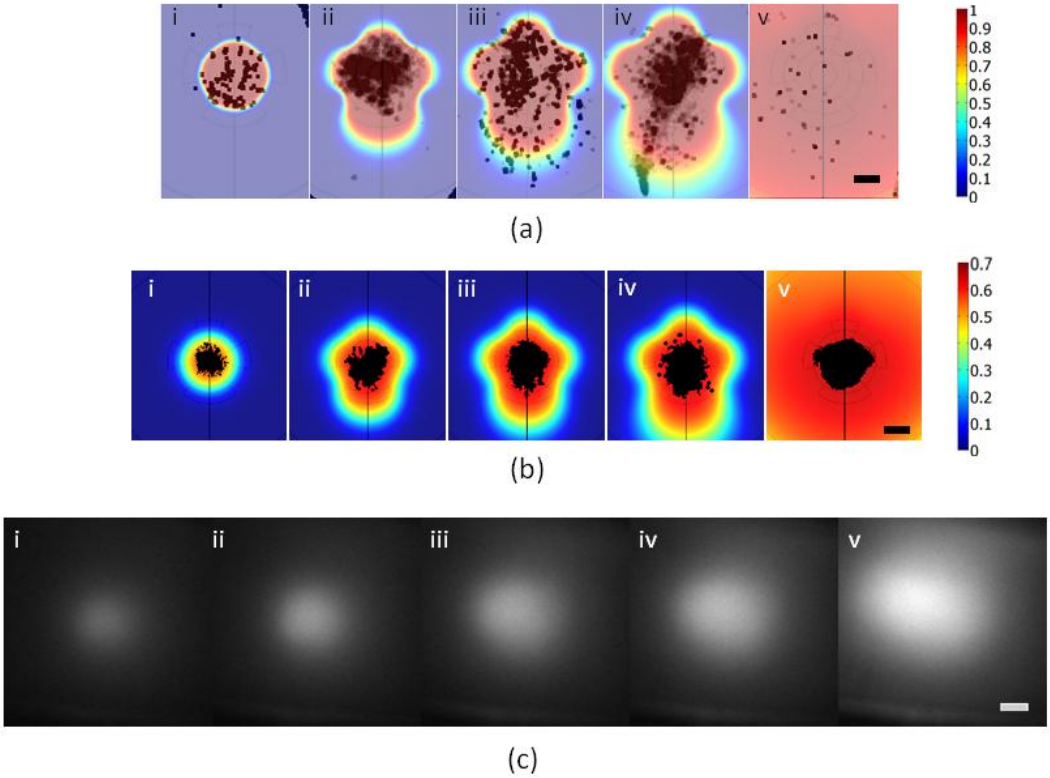

Figure 3.5: Plume profile inside a slice.

(a) Trypan blue staining experiment results (black dots) overlaid on the predicted concentration profiles (colormap) at the bottom of the brain slice for five different injection to suction flow rate ratios. (b) Methylene blue staining results overlaid on the predicted concentration profiles within the slices (at 45µm from the bottom of the slice). (c) Fluorescent images taken from the top of the slices. The scale bar corresponds to 100µm.

Fig. 3.5b shows the predicted concentration profiles at 45 μm above the slice bottom surface. This location is chosen accounting for the fact that the thickness of the surface dead cell layers in rodent brain slices is estimated to be typically 15-70 μm(Teyler 1980; Gholmieh et al. 2006). Images from the methylene blue staining experiments, where the stained cells are represented once again as dots, are overlaid on top. Overall, the areas occupied by the stained cells are smaller than those for the trypan blue experiments. This is because methylene blue only stains intact viable cells deeper into the slice where the concentration profiles are narrower.

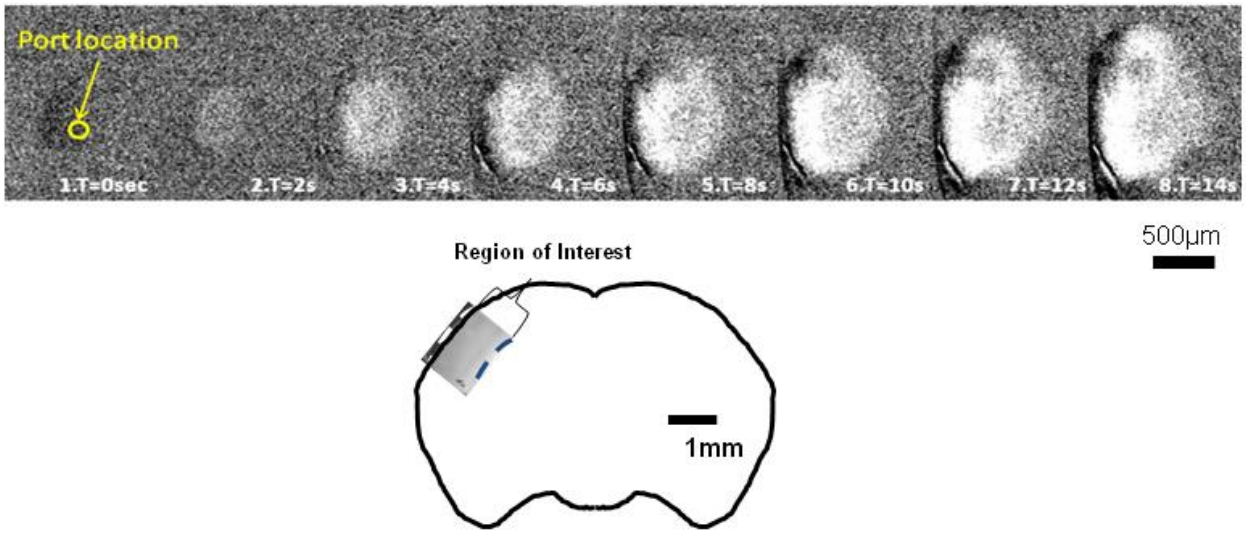

Figure 3.6: Temporal montage of a CSD wave initiated by local chemical stimulation using the present brain slice chamber (time from 0 second to 14 second). The lower inset shows the location of the cortex region on a brain slice.

3.3.4 Local induction of cortical spreading depression (CSD)

Cortical spreading depression (CSD) is a self-propagating wave of cellular depolarization in the cerebral cortex. CSD is implicated in migraine headache, stroke, and brain injury and has therefore been a subject of extensive study by the neuroscientific community(Somjen 2001; Charles and Brennan 2009). During a CSD event, neurons and glia undergo a massive regenerative depolarization(Shinohara et al. 1979; Somjen 2001). Because of the energetic expense of regenerating functional ionic gradients after such a depolarization, only a healthy brain slice will support multiple CSD inductions. The ability to induce multiple CSD events is therefore considered a biologically relevant measure of the viability of brain slices.

We chemically induce CSD in brain slices by locally injecting a 1M solution of KCl through the fluidic port. The experimental condition is similar to that used for Case 2 (or condition i in Fig. 3.5): mean injection velocity: 0.0042 m/s; mean suction velocity: 0.0180 m/s). The injection flow is sustained less than five minutes for each CSD event. The elevated extracellular $[K^+]_e$ triggers a concentric depolarization of neurons and glial cells originating from that locus. The spreading depolarization causes cells to swell, resulting in changes in their optical properties. The spreading can therefore be observed optically as a dark ring spreading from its onset point, as illustrated in Fig. 3.6.

Using the current slice chamber, we can elicit multiple CSD events in each slice, confirming excellent slice viability. The time interval between successive CSD inductions is approximately 10 minutes, consistent with previous observations(Somjen 2001). To our

knowledge this is the first demonstration of controlled, noninvasive, focal induction of CSD in brain slices. Other methods either require perfusion over large sections of a slice(Kasser et al. 1988; Tao 2000) or invasive techniques such as glass micropipettes(Ling and Gerard 1949; Myers 1967; Tao 2000; Kottegoda et al. 2002). Moreover, conventional noninvasive techniques cannot control the number of CSD events elicited(Kasser et al. 1988; Tao 2000). We are able to induce multiple CSD events with controlled timing, and do not observe any events other than the ones we trigger.

The threshold concentration of chemical stimulants for CSD induction can be used as a measure of brain excitability in migraine models[41]. Because of precise control over molarity of the K^+ solution, our preparation will allow more fine-grained determination of CSD thresholds than previously possible. The results of an on-going systematic CSD induction study will be reported in a future publication.

3.4 Summary

A novel microfluidic chamber is demonstrated with the ability to simultaneously inject and withdraw a fluid to stimulate a brain slice in a locally controlled manner. Fluorescence imaging, particle tracking velocimetry, and cell staining experiments are performed to demonstrate spatial confinement of injected chemicals. The experimental results compare well with numerical simulation results.

Our work establishes approaches to characterize brain slices under localized chemical stimulation and provides an initial demonstration of how these approaches improve the

characterization of a neurophysiological event. It also motivates further work to implement microfluidic devices for *in vivo* studies and therapeutic treatments of neurological diseases.

CHAPTER 4 Minimum Conditions for the Induction of Cortical Spreading Depression

Cortical spreading depression occurs during various forms of brain injury such as stroke, subarachnoid hemorrhage, and brain trauma, but it is also thought to be the mechanism of the migraine aura. It is therefore expected to occur over an apparent range of conditions including the awake behaving state. Using a microfluidic device in a mouse brain slice model, we varied extracellular potassium concentration as well as the area exposed to increased extracellular potassium to determine the minimum conditions necessary to elicit CSD. We found a strong correlation between the threshold concentration and the slice area exposed to the increased extracellular potassium concentration. Our results show that CSD is inducible under the conditions that might be expected in migraine aura as well as those related to brain trauma.

4.1 Background

Cortical spreading depression (CSD) is a fundamental response to brain injury. A propagated wave of massive gray matter depolarization, CSD has been incontrovertibly shown to occur in human brain insults including stroke, subarachnoid hemorrhage, and trauma (Lauritzen et al. 2011). CSD is also highly conserved in phylogeny, occurring in all mammals tested, as well as birds, reptiles, fish, and amphibians (Marshall 1959; Young 1980). CSD-like events even

occur in insects in situations of systemic stress, and appear to convey an adaptive advantage (Rodgers et al. 2007; Armstrong et al. 2009).

Yet there is very strong circumstantial evidence that CSD also occurs in migraine, a condition in which no apparent brain injury or massive systemic stress occurs (Olesen et al. 1981; Woods et al. 1994; Cao et al. 1999; Bowyer et al. 2001; Hadjikhani et al. 2001). Moreover, unlike in stroke, subarachnoid hemorrhage, or trauma, humans undergoing migraine aura are conscious and able to report their experience (Russell and Olesen 1996). This implies that CSD must be inducible under conditions of relative physiological normalcy.

Previous models of CSD use massive ionic, metabolic, or traumatic insults that would not be compatible with the awake, behaving and apparently uninjured state of migraine (Somjen 2001; Charles and Brennan 2009). It is important to know whether there are conditions that would allow induction of CSD without overt injury.

A first step in understanding the 'naturalistic' induction of CSD is to know the minimum criteria that will set off this all-or-none event. The pioneering work of Matsuura and Bureš (Matsuura and Bureš 1971) suggests that a surprisingly large volume of tissue – approximately 1 mm^3 – is required to initiate CSD *in vivo* in rat brain. However, their techniques did not allow a precise quantification of either the volume of tissue depolarized, or the ionic concentrations necessary to trigger the phenomenon.

We utilized the microfluidics-based device which allows precise local control of chemical environments of a brain slice. By varying the extracellular K^+ concentration $[K^+]_e$ and the area of brain slice perfused with high-K^+ solution, we were able to obtain minimum conditions required for CSD induction at different concentrations and volumes. We find that

CSD is inducible under different physiologically plausible parameters, with minimum volumes of depolarized tissue necessary under $[K^+]_e$ predictable in trauma, and significantly larger volumes required under $[K^+]_e$ that might be expected to occur without injury. Our data thus defines a framework of minimum necessary conditions upon which the physiologically realistic modeling of CSD (*in silico*, *in vitro*, and *in vivo*) can proceed.

4.2 Materials and Methods

4.2.1 Microfluidic brain slice chamber

The microfluidic device and experimental setup is shown in Fig 4.1A and B (Ch. 2 and 3). The device(Tang et al. 2011) consists of a microfabricated polydimethylsiloxane (PDMS) structure which supports the brain slice and allows for focal delivery at different locations on the slice. The slice rests on a network of posts which allow bath perfusion of the underside as well as the top surface. At selected locations, the posts are replaced by assemblies of injection and suction ports. Each injection port is surrounded by several suction ports to realize a confined chemical plume at each port. Center injection port radii were 50, 75, 100, 125, 140, 180 and 250 μm.

Underneath the post and port layer are fluidic delivery and removal microchannels, which connect to a peristaltic pump and suction pump, respectively. Multiple silicone tubings (ID: 1/8") were bonded to the inlets and outlets of the microchannels. A syringe pump (sp100i Pump; WPI, Sarasota, FL) was used to deliver artificial cerebrospinal fluid (ACSF) solution with set $[K^+]_e$

into the injection port. A vacuum pump (BUCHI V-700, New Castle, DE) with a feed-back pressure control module was used to adjust suction flows, with mean velocities between 0.01 m/s to 0.1 m/s, and achieved a controlled confined plume of a potassium-rich ACSF solution[15].

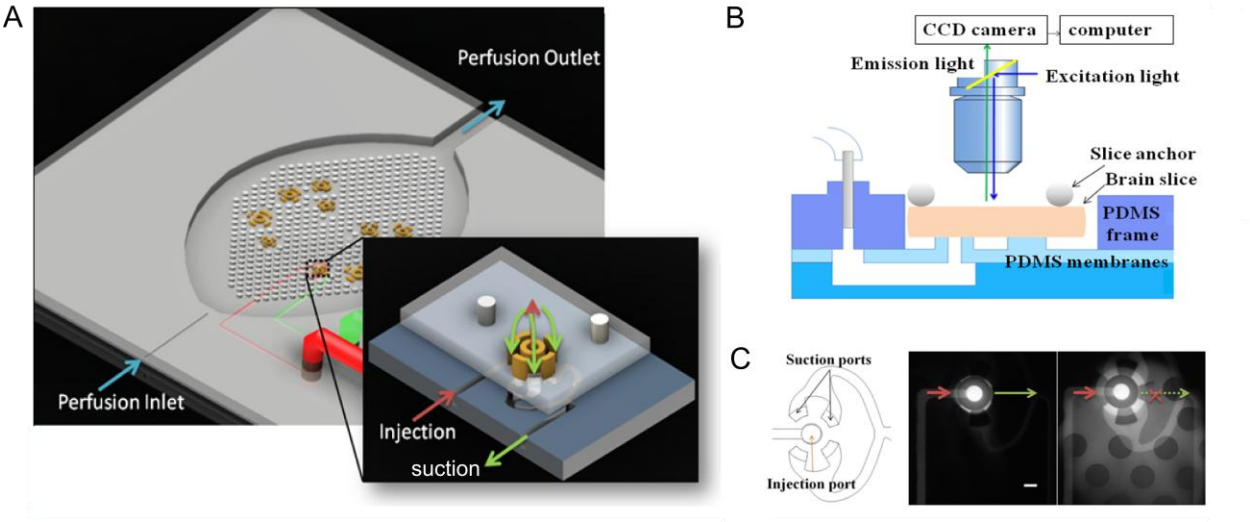

Figure 4.1: Schematic of device, experiment setup and operation of device.

(A) Conceptual view of the microfluidic chamber for localized brain slice stimulation, blue arrow represents the slice perfusion direction. An array of micro-posts supports the brain slice and allows bath perfusion of the underside as well as the top surface. Selected posts are replaced by assemblies of injection and suction ports. Inset showing one injection/suction port, red arrow represents the injection flow, green arrow represents the suction flow. (B) Schematic of the experiment setup showing the chamber is integrated with epifluorescence imaging. (C) left: top view of one injection/suction port; middle and right: fluorescence images of the injected flows with (middle) and without (right) suction. Scale bar, 100 μm.

4.2.2 Brain slice preparation and maintenance

Experimental protocols were approved by the UCLA Chancellor's Animal Research Committee. Male C57Bl/6 mice (25–30 g) were deeply anaesthetized with isoflurane and decapitated. The brain was rapidly removed and immersed in room temperature high sucrose low sodium ACSF of the following composition (in mM): 216 sucrose, 2 KCl, 2 $MgSO_4$, 1.25 NaH_2PO_4, 2 $CaCl_2$, 1 $MgCl_2$, 26 $NaHCO_3$, 10 glucose bubbled with 95% O_2, 5% CO_2. The brain was then glued to a stage and coronal slices of 400 µm thickness were cut in ice-cold oxygenated sucrose solution with a standard vibratome (MA752 Motorised Advance Vibroslice, Campden Instruments). The slices were then incubated in an oxygenated ACSF solution (in mM: 125 NaCl, 3 KCl, 1.25 NaH_2PO_4, 2 $CaCl_2$, 1 $MgCl_2$, 25 $NaHCO_3$, 10 glucose) at room temperature for at least one hour before the experiments.

4.2.3 Induction of CSD in brain slices

Brain slices were transferred from the tissue culture incubator to the microfluidic recording chamber kept at 32 ± 1 ^oC, with a continuous ACSF bath perfusion fluid bubbled with 95% O_2 and 5% CO_2. This bath solution was delivered to the chamber using gravity at 2 ml/min. A piece of filter paper (not shown) was placed at the outlet to minimize flow fluctuations. The perfusion rate was measured by mass before the experiment, and chamber temperature was monitored throughout the experiment to verify that the flow rate had little variability during recording (32 ± 1 ^oC). Also, measurements and simulation data showed that the bath perfusion flow rate underneath the slice was two orders of magnitude smaller than the local injection or

suction rates (< 0.117 mm/s vs. 25 mm/s), allowing us to conclude that variation in bath perfusion rate would be very unlikely to affect port injection and suction. The slice was positioned such that the pial surface was aligned to the perimeter of the suction port. This allowed systematic comparison of different port sizes over the same anatomy. A platinum wire (300 μm in diameter) was placed on top of the slice, but away from the gray matter area of interest, to immobilize the slice.

CSD was induced by injection of a high-K^+ ACSF solution containing different molarities of KCl substituted for equimolar NaCl. The molarities were 12, 15, 25, 30, 40, 60, 70, 80, 120, 130, and 140 mM above normal ACSF K^+ concentration; thus total K^+ concentrations were 15, 18, 28, 33, 43, 63, 73, 83, 123, 133 and 143 mM. A small amount of fluorescein (< 0.1%) in the ACSF solution allowed visualization and measurement of the plume.

CSD thresholds were determined by varying potassium concentration and stimulation plume size. Plume size was varied by changing the microfluidic port size. Each brain slice was tested with one port size; at least 3 experiments were conducted at each port size and concentration. In selected experiments, ports were not used and instead $[K^+]_e$ over the whole slice was changed via bath perfusion.

The baseline $[K^+]_e$ of 3 mM was increased in 5 to 10 mM steps for two minutes or until CSD was observed. Following that, a confirmative experiment was conducted with either a lower concentration or a smaller plume size than the previous experiment condition for two minutes to confirm that no CSD would be induced below the threshold detected. At the end of the experiment, the viability of the slice was confirmed by a successful CSD induction with supra-

threshold volumes (elicited by stopping suction at the suction ports, allowing a larger plume to form). After each injection test, the injection port was flushed with oxygenated ACSF and the slice was allowed to rest for 10 minutes before a new concentration was tested.

In order to show that there was not a systematic bias inherent to ascending thresholding, we also performed thresholding that began at maximum concentrations and descended until a minimum threshold level was reached. We observed no difference in the thresholds reached with these techniques (12 descending to 4 ascending experiments) and thus the data were pooled for further analysis.

The brain slice was imaged using a 4x objective (UPlanSApo, Olympus America, Melville NY) coupled to a high sensitivity camera (Mightex CCE-B013-U, Pleasanton, CA). Blue LED light (470 nm, half width 25 nm; Luxeon III, Phillips Lumileds) was passed through a filter cube (excitation 470 ± 20 nm, dichroic 505 nm, emission > 515 nm; Chroma Technology) for epifluorescence imaging. A green LED (500-540 nm) directly illuminated the slice for optical intrinsic signal imaging. Images were acquired at 2 Hz; pixel size was 2.2 μm.

During thresholding, epifluorescence and reflected light imaging were alternated to allow detection of the fluorescent plume as well as the intrinsic signal changes caused by CSD. One frame of epifluorescence was collected for every 60 frames of intrinsic signal until CSD was detected, at which point imaging continued with intrinsic signal until the CSD wave had propagated across the imaged region.

4.2.4 Two-photon laser scanning imaging

Two-photon laser scanning microscopy (2PLSM) was performed to determine the plume volume inside the brain slice. Experiments were performed using an upright microscope Sutter movable objective microscope coupled to a Ti:sapphire laser (MaiTai HP, Spectra Physics, CA, USA). A water-immersion objective (Carl Zeiss W Plan-Apochromat 20x/1.0 DIC) with high numerical aperture was used. When necessary, two channels were simultaneously acquired using Chroma filters (535/50nm (green) and 610/75nm (red)). Scanimage (Pologruto et al. 2003) was used for controlling the miscroscope and for recording of the images. The laser was tuned to 810 nm for FITC-Dextran and sulforhodamine 101 excitation.

For these experiments, brain slices were cut in 300 μm thickness. The reduced thickness permitted us to scan images under the slice as well. Slices were incubated in ACSF with 1 μM sulforhodamine 101 (SR101 Invitrogen , Carlsbad, CA) added at 32 ^{o}C for at least 30 minutes. SR101 labeled astrocytes throughout the thickness of the slice (Nimmerjahn et al. 2004) allowing anatomical registration. Ports used in two-photon experiments had center injection radii of 125 μm. FITC-dextran (3000-5000 m.w. Sigma) was added to ACSF for visualization of the injected plume. Before each scan, the top of the brain slice and the fluid port were located respectively. The location of slice top was determined by lowering the microscope focus until the first image of SR101 stained astrocytes (red) became visible. The whole slice was then scanned from its top to about 100 μm below the port top surface in 10 μm increments. Laser power was adjusted to compensate for the light intensity decays with depth into the slice.

4.3 Data analysis and statistics

4.3.3 Measurement of plume size

The last fluorescent image before CSD induction was analyzed to determine the plume size. The transverse intensity distributions of the fluorescent image assembled well in Gaussian profile. Because of the complexity of light diffraction and scattering within the brain tissue, the plume size was plotted in two forms: with no slice coverage (bare) and with slice coverage (covered). For the former case, the fluorescent intensity slope was steep and the error in determining the size was within 2 μm (2 ~ 3 pixel). For the latter case, we determined an intensity threshold to define the plume edge in preliminary experiments (n = 6). In those experiments, we placed the port in a way that the ejected plume was only partially covered by a brain slice. The thresholding was established so that the edge obtained with the selected threshold from the plume covered by the brain slice matched that extracted from the uncovered portion of the plume at the pial surface. A 50 percent intensity threshold was experimentally determined to be most consistent with the uncovered plume boundaries, and was applied for all experimental data. The plume area was analyzed and radius was calculated assuming a circular plume shape.

4.3.4 Calculation of affected cortical volume with simulation

3D multi-physics simulations using finite element method (FEM) were performed to predict the concentration profile inside the brain tissue for different combination of injection and

suction flow rates, as previously described[15]. Briefly, Navier-Stokes equations were solved to calculate the velocity field around the fluid port. The time-dependent convection-diffusion equation for mass transport was then solved for the concentration profile inside the slice as a function of time. To account for the hindered diffusion due to ion movement in the tortuous pathways, the diffusivity of K^+ in free medium (2×10^{-9} m^2/s) was divided by λ^2 to represent the apparent diffusion coefficient (ADC),

$$D_{Apparent} = \frac{D}{\lambda^2} \tag{4.1}$$

where λ is the tortuosity of the brain ECS. The value of λ for calculating diffusion coefficients of the injected molecule (fluorescein + K^+-ACSF) employed in the model was 1.8 and 2.2 taken from the upper and lower limits of ADC reported in previous work(Nicholson 1993; Nicholson and Tao 1993; Binder et al. 2004; Syková and Nicholson 2008; Zador et al. 2008).

To calculate the affected cortical volume corresponding to each experiment, we first matched the plume size extracted from the epifluorescence image to the larger-than-zero concentration area at the slice bottom from simulation to obtain the combination of injection and suction flow rates. Then the simulation was performed under the specific condition for each experiment with the matched flow rates and observed time from the beginning of injection to the initiation of CSD. The concentration threshold selected for comparing the affected volume of brain was 15 mM. This value was determined from experiments as the minimum concentration that will induce CSD in the slices.

4.3.4 Measurement of plume volume

The excited fluorescence intensity was observed to decay with depth in our scanned images. To compensate for the decline of power with imaging depth z induced by the light scattering in slice (Helmchen and Denk 2005), we firstly performed normalization of the image intensities at different depths. The image stack acquired in the red channel showing SR 101 was taken as a reference. The basic assumptions of this method were that the fluorescent astrocytes signals were uniform throughout the thickness of the brain slice and the red and green channels scaled in a similar manner with depth. The red channel images were normalized to reach the same mean fluorescent intensity. Assuming both channels scale similarly, the green channel images are normalized in a way identical to the red channel images. An alternative normalization method was performed for comparison with the red channel reference method. The fluorescence signal decays as a function of the applied laser power and depth and is described as,

$$F_{2PLSM} \propto P_0^2 \times e^{-2z/l_s} \tag{4.2}$$

where F is the fluorescent intensity, P_0 is the laser power applied, z is depth of scan and l_s is the mean free path describing the scattering properties of the tissue (Helmchen and Denk, 2005). The image intensities were scaled based on the theoretical light intensities calculated from Equation 0 where the P_0 and z are recorded simultaneously with scanning. The approximate value for l_s was 143 μm which is taken from a separate scan performed prior to the experiment. We then determined a threshold for the FITC-dextran plume boundary. We assumed that at the slice bottom the plume bore a size determined merely by the microfluidic port geometry. The intensity

satisfying the criteria at the slice bottom was used to threshold the rest of the images for volume extraction. Linear interpolation was assumed in between frames with 10 μm steps. To compare the measured and simulated volume, we found the plume area at slice bottom and derived the corresponding concentration from the empirical threshold-area curve we obtained (see results below).

4.4 Results

4.4.1 Reliability of CSD induction and recording

CSD waves were successfully induced by locally injecting potassium rich ACSF onto cortical layers of mice brain slices. CSD was recorded as an approximately concentric propagating wave of decreased, followed by increased, white light reflectance (Fig 4.2C), propagating out from the port site at a speed of approximately 3mm/min (median: 3.0, 25 percentile: 2.3, 75 percentile: 3.7; unit: mm/s), approximately 30 seconds (median: 30 s, 25 percentile: 19 s, 75 percentile: 71 s, range: 5 ~ 232 s, n = 75) after the high-K^+ ACSF solution reached the brain slice.

In preliminary experiments we used direct current field potential recordings (Fig 4.2B) to verify that the optical signature of brain slice CSD was indeed accompanied by its electrophysiological correlates (ACSF-filled 2 MΩ resistance glass electrode advanced 200 μm into slice, A-M Systems 700 amplifier, band pass 0-1KHz, digitized at 1KHz).

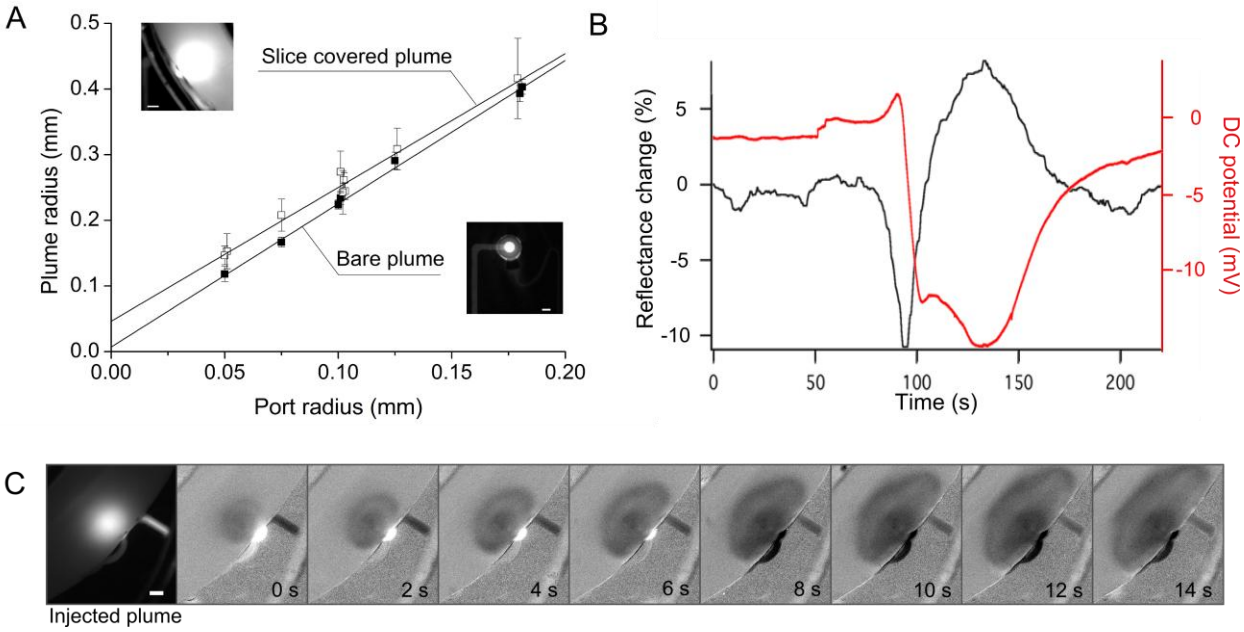

Figure 4.2: Optical characterization of CSD induced by a localized high-K^+ plume.

(A) Plot of the dependence of plume radius on port size, showing a strong linear relationship for plume sizes both with (empty squares) and without a brain slice (filled squares) in the chamber. Bar representation 100 μm. (B) Simultaneous recording of the extracellular DC potential (red line) and reflectance change (black line) during cortical spreading depression. Optical signals were measured near the electrical recording site. (C) Optical intrinsic signal changes during a CSD wave triggered by a localized injected plume with high-k^+ ACSF solution. Images show the fluorescent plume used for stimulation (first image from left) followed by the typical optical changes during the propagating CSD wave registered every 2 s for 14 s. Scale bar, 200μm.

A minimum of 3 ~ 4 waves could be induced in the same slice at same location. CSD was only induced during superfusion of high-K^+ ACSF solution; we never observed spontaneous CSD induction (n = 242 inductions, 102 experiments).

4.4.2 Control of exposed area with microfluidic device

It is difficult to localize and control fluid flow in a perfused slice chamber: the use of suction ports around the injection port provided this control. Fig 4.1c shows ACSF plumes (labeled with fluorescein) in the perfused chamber before and after activation of suction ports: the plume is effectively controlled both with and without the brain slice in the chamber. Confined plumes were also much more regular in shape (circular) when suction was activated. Once control over plume parameters was established it was possible to systematically vary port size. Fig 4.2A shows plume radius plotted against port size, showing a strong linear relationship for plume size both with and without a brain slice in the chamber. Replicability of plume size was also excellent (Fig 4.2A).

4.4.3 Minimum conditions for CSD induction

Fig 4.3 shows the injected potassium concentration threshold as a function of the covered plume size. The horizontal and vertical asymptotes express minimum concentration and radius, respectively, necessary to induce CSD. Fitting $[K^+]_e$ and threshold plume size threshold data at physiological levels ($\leq$ 145 mM) yielded a relationship depicted using Equation. 4.3 (Fig 4.3).

$$C \times r^{2.044} = 3.614 \tag{4.3}$$

where C is extracellular potassium concentration $[k^+]_e$ and r is the plume radius. Linearization by taking logarithm of both concentration and plume radius was performed to fit the data (R-squared value for the linear fit is 0.921). The result suggests that the minimum CSD induction condition is determined primarily by the area of the brain slice (or "thickness" of cortex) exposed to higher $[K^+]_e$. CSD is induced once excess K^+ ions diffuse sufficiently into the brain slice, past dead cell layers on the slice surface. Small variations on the induction time (19 ~ 71 seconds) may be indicative of variations in the thickness of surface dead cell layers. At lower concentrations, the plume sizes scattered in a wider range than at high $[k^+]_e$, which suggested a dominant role of the upper cortical layers. That is, involving more cortical neurons at layers close to the white matter may have little influence on the threshold. The anisotropy of cortical layers in inducing CSD will be discussed further in detail in our following work (Bogdanov et al, manuscript in preparation).

The minimum concentration required to evoke CSD was approximately 15 mM K^+, which was achieved with plume radii greater than 0.5 mm. From Equation 2, the minimum size for this concentration was also derived to be around 0.5 mm. This result was consistent with values independently determined by bathing the whole slice with potassium rich ACSF. The concentration threshold increased rapidly for port radii below 300 μm. The minimum port radius at which we could induce CSD at physiological concentrations (≤145 mM; or intracellular K^+ concentration) was 75 μm. We were unable to elicit CSD at physiological concentrations with smaller port radii (50 μm, n = 9). This smallest port size could only induce CSD at a concentration greater than 200 mM.

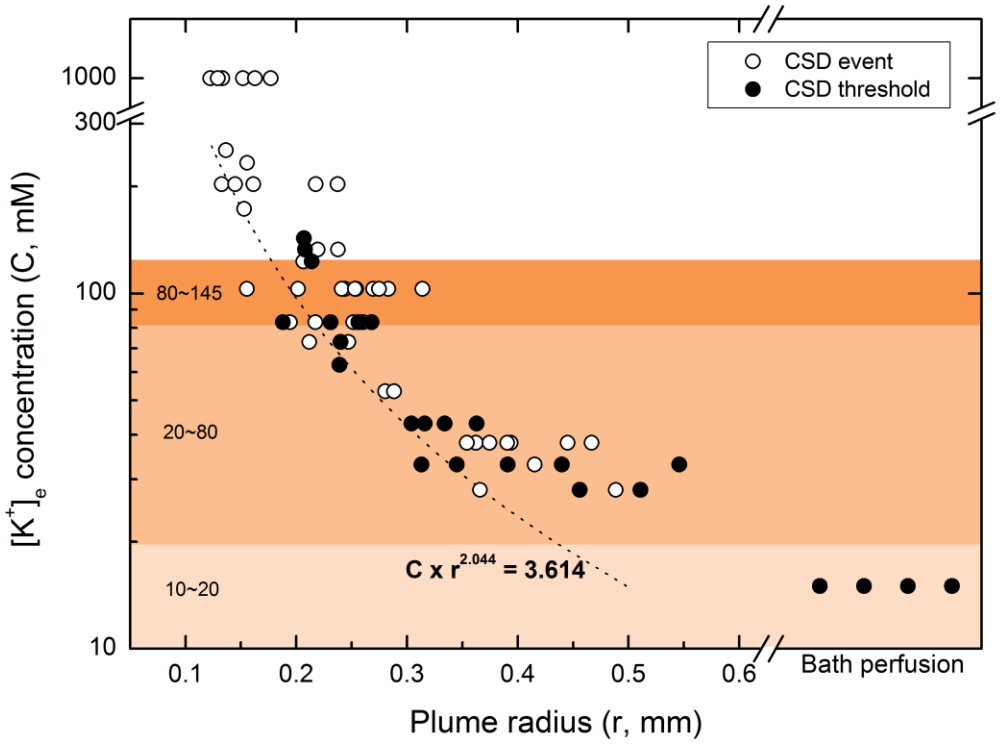

Figure 4.3: Plot of minimum condition for CSD induction.

CSD is induced by a confined high-K^+ ACSF solution with a minimum stimulation size shown in filled dots. Open circle shows successful CSD inductions with leaky plumes. Minimum concentration to induce CSD is 15 mM. The size of the stimulus is beyond the total thickness of the cortex. Dashed line is the best fitting line of circles lying on the envelope of the data pool indicating the minimum condition for CSD induction and shows the product of concentration and area is nearly constant.

4.4.4 Minimum tissue volume for CSD induction

We stimulated the slice under-surface with known concentrations of KCl. However, one cannot expect that these concentrations were achieved throughout the thickness of the slice. The concentration achieved is inside the slice expected to be a function of the concentration at the slice interface, the apparent diffusion coefficient of the solute, cellular clearance mechanisms, and the time of exposure. The diffusion coefficient is a function of the tortuosity of fluid flow within the tissue.

We first used two-photon laser scanning microscopy to determine the plume size inside the brain slice *in situ* (Fig 4.4). FITC-dextran mixed in ACSF was applied through the port and the real time plume was revealed by reconstructing the z-scanned images. The thresholded volume was displayed in Fig 4a.

We then applied finite element methods (FEM) to predict 3D concentration profiles (Fig 4.4) using the two ADCs. The light intensity decay map and the concentration isosurfaces were plotted together in Fig 4b. The two profiles show a resemblance for intensity change. The thresholded volume extracted from two-photon experiments was close to the 10% of the applied solution concentration in numerical simulation. The column highlighted in Fig 5 shows the predicted volume for the minimum concentration (15 mM), which is within a range of 0.01 ~ 0.03 mm^3. The predicted volume with 10 and 50 % of the applied solution concentration as the threshold is also shown as a reference.

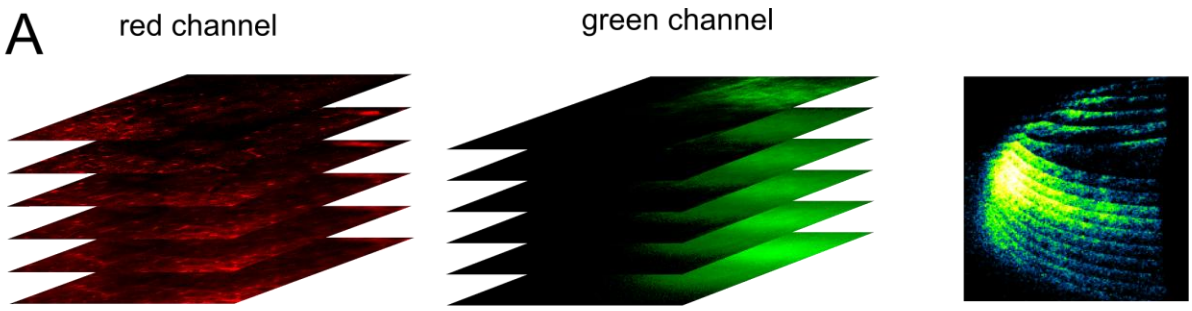
A
red channel
green channel

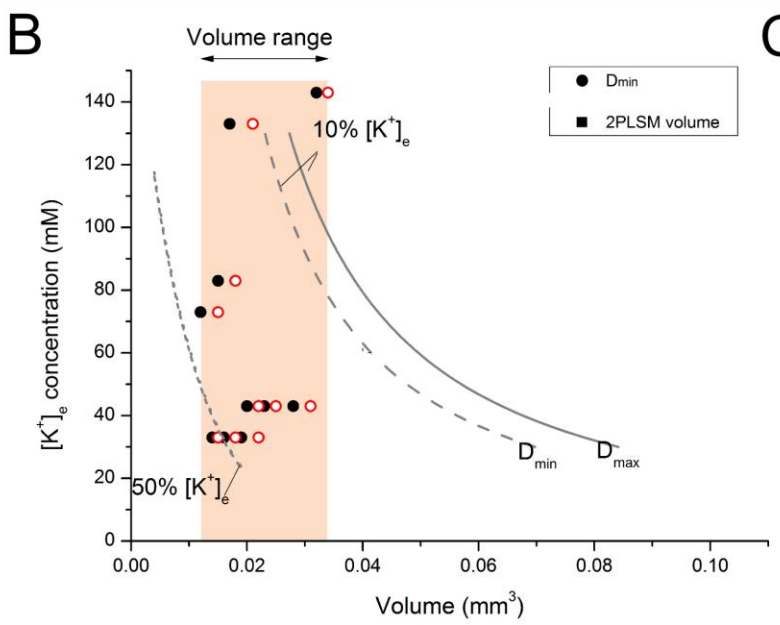
B
Volume range
Dmin
2PLSM volume
10% [K+]e
50% [K+]e
Dmin
Dmax
[K+]e concentration (mM)
Volume (mm3)
0
20
40
60
80
100
120
140
0.00
0.02
0.04
0.06
0.08
0.10

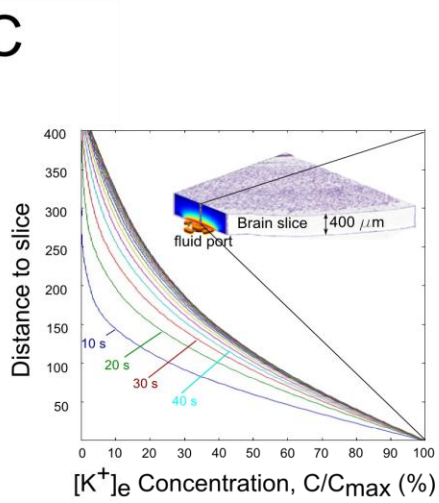
C
Brain slice
400 μm
fluid port
10 s
20 s
30 s
40 s
Distance to slice
[K+]e Concentration, C/Cmax (%)
50
100
150
200
250
300
350
400
0
10
20
30
40
50
60
70
80
90
100

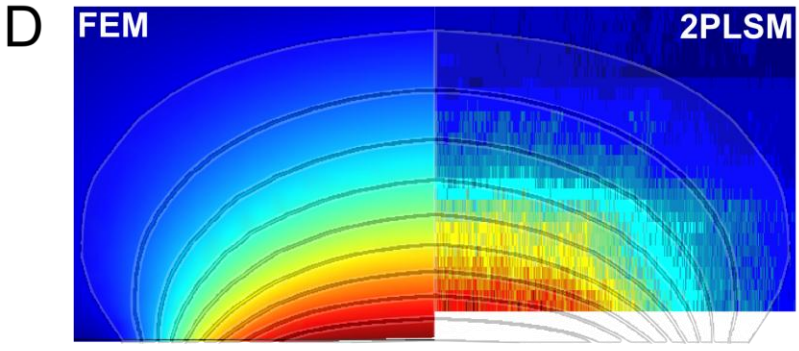
D
FEM
2PLSM

Figure 4.4: Quantization of simulated minimum volumes and measured plume sizes for CSD induction.

(A) Volume determination using 2PLSM and numerical simulation. Left: red channel images were used for locating slice depth. Middle: green channel images are scaled and based on the z location and intensity applied. Right: 3D reconstructed plume thresholded by an arbitrary intensity. (B) Circles show the volume from numerical simulation representing the corresponding volume for each data in Figure 3 (filled circles) assuming pure diffusion in extracellular space. Cortical volume with concentration higher than 15 mM is plotted. Lines are showing volumes with concentration higher than 10% and 50% with respect to the applied solution concentration. Two ADCs were selected to describe the boundaries of the possible ion diffusion activity (filled and open circles). (C) Simulated extracellular potassium concentration is plotted across the slice thickness at the port center location as a function of time. The concentration at each location is elevated as a function of time as a result of a continuous supply of high-k^+ solution at the slice bottom surface. A schematic diagram of the slice model is shown in the inset. Concentration is plotted along the dotted line above the port center. (D) Fluorescent intensities throughout the thickness of the slice (right panel) and concentration profiles from numerical simulation (left panel) superimposed with concentration contours from 10% to 90% of the applied solution concentration suggest a close match of intensity/concentration gradients. The depth different is accounted by the surface dead cell layer which occupied certain slice thickness that would not shown in the SR 101 staining results.

The volume invaded by the FITC-dextran plume was 0.043 ± 0.003 mm^3 (mean ± std. dev., n = 4, Fig 4.4). The cortical volume was large as compared to the numerical predicted volume (~0.04 mm^3 vs. 0.02 mm^3). The enlargement in volume was probably due to the time difference in between two-photon experiments and CSD induction experiments. The total laser scanning time was about 0.5 ~ 1 minutes longer than the CSD induction time measured in previous experiments. The time evolved concentration profile was plotted in Fig 4.4 as a result of diffusion. Due to a longer diffusion time, the total volume of the fluorescein plume was larger.

4.5 Discussion

CSD is advanced as the physiological mechanism behind the migraine aura. However it is surprising that such a massive ionic and metabolic event – incontrovertibly seen in conditions of brain injury – could be generated in the awake uninjured brain.

We designed our experiments to address the biological feasibility of CSD under physiologically realistic conditions. In contrast to most CSD models(Aitken et al. 1998; Ayata et al. 2006; Brennan et al. 2007) we focused on $[K^+]_e$ that could be expected *in vivo*, in a range whose maximum was approximate intracellular $[K^+]$. This maximum concentration is relevant to situations such as brain trauma or stroke, where cellular lysis occurs. The lower limits of the range were designed to test the "K^+ ceiling" – levels of extracellular K+ ranging from 10 ~ 20 mM, beyond which both neuronal and vascular behavior changes dramatically (Somjen et al. 1976; Heinemann and Lux 1977; Somjen 1979; Knot et al. 1996). These concentrations are achievable *in vivo* during pathological states, such as seizure (Heinemann et al. 1977;

Heinemann 1986), that are recoverable without apparent cellular injury. Intermediate levels (30 ~ 80 mM) are seen during passage of the CSD wave (Somjen 2001), and are also likely relevant to tissue in the vicinity of brain injury such as a contused or infarcted region.

Minimum volume to induce CSD was first studied by Matsuura and Bureš[14] based on their experiments using temporal summation of two chemical stimuli in a rat model *in vivo*. The minimum diameter of depolarized tissue was predicted to be 600 and 960 μm with a minimum $[K^+]_e$ between 12 and 45 mM, and time to onset of CSD of approximately 60 seconds.

Whereas minimum concentrations and time of onset agree well between both models, our results predict a much smaller minimum volume of depolarized tissue. This may be due in part to a difference in geometric configuration. In our experiments, K^+ ions diffused primarily into brain slices (or parallel to the cortical surface) and the surface area (or cortical depth) was more or less pre-determined by our plume sizes. More isotropic diffusion is expected in *in vivo* experiments. The difference between our slice experiments and the previous *in vivo* experiments may therefore highlight the significance of depth anisotropy in CSD induction.

It is also possible that differences in preparation (rat vs. mouse brain, *in vivo* vs. *in vitro* preparation) could account for these differences. In addition, the use of two closely spaced 200 μm diameter capillaries by Matsuura and Bureš is likely to have caused tissue damage; as dead tissue does not initiate or propagate CSD (Somjen 2001) larger total volumes of tissue would have to be depolarized to achieve CSD ignition. Moreover, an advantage of our preparation is that we were able to directly control and visualize the area exposed to depolarizing stimulus, likely making our estimates of depolarized volume more precise. Definitive resolution of these

differences will require accurate measurement of plume size and $[K^+]_e$ *in vivo*, perhaps with a combination of two-photon microscopy and K^+ sensitive dyes or electrodes.

If CSD occurs in awake behaving humans, as is proposed for the migraine aura, it must occur under conditions that do not result in either incapacitation or lasting injury. The volume of depolarized tissue predicted from our experiments is small enough that transient, focal alterations in perfusion or metabolism might be sufficient to set off CSD. In this context it is interesting to note that our predicted minimum volumes of tissue depolarized are similar to the predicted volume of a cortical column (Mountcastle 1997) or penetrating artery territory (Woolsey et al. n.d.). One could speculate that a discrete sensory column exposed to excessive stimulation, or a single penetrating artery undergoing reversible spasm, might be sufficient to cause CSD but not result in lasting tissue damage.

The control we achieve over the ionic and fluidic environment was not possible without a brain slice preparation. However, an obvious limitation of this approach is that the vascular changes that accompany and likely influence CSD were not sampled. Vascular activity is particularly important because of its homeostatic role *in vivo*, and because cerebral arterioles constrict rather than dilate at $[K^+]_e$ which induce CSD (Knot et al. 1996). This means that vascular delivery and clearance of metabolites is compromised at the precise $[K^+]_e$ at which neurons and glia are entering a critical transition to depolarization. Implications will need to be tested *in vivo*, but one would predict that thresholds, or minimum areas of depolarization, could actually be lower in the presence of a functional vasculature. On the other hand, vascular clearance of $[K^+]_e$ could slow the approach of $[K^+]_e$ to threshold values, and thus have opposite effects.

Our use of a mouse model may also not completely mimic conditions expected in humans. Mouse neural and cellular density is greater than that of humans, and the neuron/glia ratio is higher (Tsai et al. 2009). The implication is that mouse tissue might support CSD at smaller volumes of tissue depolarized than human tissue. The fact that mice are lissencephalic while humans are gyrencephalic is likely not relevant to our slice experiments, but has implications for CSD induction and propagation (Dahlem and Hadjikhani 2009).

For computational simplicity and limitation in real time $[k^+]_e$ measurement capabilities, our model considered diffusion the only mechanism for K^+ ion distribution in the ECS. Other physiological K^+ regulation mechanisms should be considered to fully predict the minimum condition for CSD induction: 1) K^+ release from neuronal and glial activity; 2) active K^+ uptake by neurons and glial cells; 3) K^+ spatial buffer by glial cells ; and 4) passive KCl uptake by glial cells (Kraig and Nicholson 1978; Largo et al. 1996; Holthoff and Witte 2000; Walz 2002; MacAulay and Zeuthen 2012). The summed effects of these mechanisms would likely lower local extracellular potassium concentration in the region at the edge of the plume. So the plume volume predicted by numerical simulation and measured by two photon experiments needed to be carefully interpreted. However, the combination of a flattened plume and short induction time for CSD argues that these effects may be minimal. A plume surface/depth diameter ratio larger than 3, and a concentration-radius curve with a linear concentration-area relationship suggests that plume volume is mainly determined by surface area. Moreover, given a short stimulation time before CSD starts (< 1min) in most of our experiments (9 out of 11), one would expect that the minimum volume for 15 mM $[K^+]_e$ will be close to the predicted value (0.01 ~ 0.03 mm^3).

To confirm this, further investigation with K^+ electrodes to determine the real concentration profile inside the slice is needed.

4.6 Conclusions

We have used a microfluidic device in mouse brain slice preparation to evaluate the minimum conditions necessary to induce CSD. We find that CSD is inducible under a range of conditions including those likely to be encountered in brain injury and those likely during awake behaving states such as migraine.

CHAPTER 5 Integration of Microfluidic Devices and Multi-electrode Arrays for Simultaneous Electrophysiology, Chemical Stimulation and Optical Imaging of Brain Slices

Optical recordings of neuronal activities provide rich information regarding the 2D characteristics of cortical spreading depression (CSD) over a large cortical region. Electrophysiology techniques, as compared with optical methods, can provide more anatomically localized measurements at higher temporal resolutions (Welker 1976). Unlike conventional glass microelectrodes, microfabricated planar multi-electrode arrays (MEAs) represent a completely noninvasive and spatially distributed tool to electrophysiological measurements. Further, a 2D electrode array provides measurements of rapid electrophysiology response over large cortical regions and allows direct correlations with simultaneously recorded optical results. In this chapter, we discuss a combination of electrophysiology measurements and optical intrinsic signal imaging to characterize CSD. Our data demonstrate that the electrode array can successfully be applied to record both high frequency signals and slow potential changes associated with CSD. Electrophysiological signals generated by CSD reliably correlates with the changes in optical intrinsic signals. Capturing electrical signals and optical images in a synchronized manner also helps identify a possible scenario for cortical spreading convulsion.

5.1 Introduction

5.1.1 Basics of electrodes

Electrodes are sensors that are sensitive to electrochemical changes in its surrounding media. In neurology applications, electrodes record the electrical properties of neurons by measuring the flow of ions introduced by neuronal activities. To detect electrical signals, the recording electrode either penetrates into or stays close to neurons in their extracellular space.

Two kinds of electrodes are mostly used in biological applications: non-polarizable and polarizable electrodes. Non-polarizable electrodes (or reversible electrodes) allow free exchange of electrons at the electrode-electrolyte interface. Classic examples are mercury electrodes and microelectrodes made by glass pipettes filled with electrolyte bridged with Ag/AgCl wires. Electrode arrays made by gluing two or more glass pipettes together have been implemented to study the propagation pattern and speed of CSD waves with high spatio-temporal resolution.

Polarizable electrodes, on the other hand, allow no net charge crossing the electrode-electrolyte interface when a current is applied. Commonly used polarizable electrodes are made of Pt, Au, Ir, W, etc. Polarizable electrodes are sensitive to their relative movement in electrolytes as it disturbs charge distributions at the electrode-electrolyte interface, generating an 'artifact signal'. Also, as ideal polarizable electrodes act like a perfect capacitor, they are not sensitive to low frequency voltage changes. In practice, electrodes have characteristics that are between the ideal non-polarizable and polarizable electrodes.

5.1.2 Multi-electrode Array (MEA)

Glass micropipettes have been widely used for electrophysiology recordings of the nervous system. When a large number of electrophysiology signals need to be recorded simultaneously, however, it is not practical or even possible to use glass microelectrodes. Besides challenges in manually handling a cluster of multiple glass electrodes, the cluster will block optical views. As a consequence, the applications of glass microelectrodes for spatial mapping have been limited.

The development of MEAs since the 1970s offers great opportunity on studying 2D network properties of brain slices. The MEAs consists of planar or extruding metal electrodes (Pt, Au, TiN, etc) isolated by an insulation material. With the advances in the semiconductor microfabrication techniques, more and more electrodes are arranged in smaller areas leading to higher spatial resolution (Chang et al. 2006). The early versions of MEA for *in vitro* applications are fabricated on a rigid substrate (i.e. glass, silicon) which supports the brain slice from bottom (Heuschkel et al. 2002). A disadvantage of this arrangement is the fixed locations of the electrodes relative to the tissue. It is challenging to pick or change the recording locations precisely, which can be easily realized in glass microelectrodes with micro-manipulators. Since it is often necessary to adjust the location of electrodes on the brain slice to study specific neuronal functions, it is favorable to have an electrode array that is easier to move relative to the slice when needed.

Neuronal responses under chemical stimulation have significant implications in drug development. As such, it is important to study the electrical responses of the brain neuronal

circuit under chemical stimulations. Due to the nature of the electrode materials, the electrodes typically used in MEAs are mostly polarizable electrodes and therefore are very sensitive to the local ion redistribution. When there is an abrupt chemical gradient change induced by local chemical stimulation, artifacts will show and sometimes conceal the meaningful neuronal signal. The interaction between chemical environments and recording electrodes prevents the integration of microfluidic techniques to MEAs if they are both on one side of the brain slice. To avoid the artifact induced by localized chemical stimulations, the chemical stimulation and electrical recording sites need to be separated.

For the reasons discussed above, we find it favorable to place the electrode array on top of a brain slice. To retain all the functionalities of a slice chamber setup, the electrode array must be mostly transparent to allow optical imaging from the top. Also, the electrode must be flexible to facilitate the conformal placement of the electrode on soft and delicate brain slices. Flexible MEA made on thin polymer membranes would meet these criteria. Taking advantage of polymer based carrier materials, previous studies reported microfabricated planar flexible electrode arrays with the total thickness down to a few micrometers (Boppart et al. 1992; Stieglitz 2001; Myllymaa et al. 2009). Such devices often consist of 10s to 100s of electrodes on flexible sheets that contact the surface of a brain to collect neural signals generated by clusters of neurons. Different insulation materials have been used such as polyimide, parylene, etc (Lee et al. 2004; Takeuchi et al. 2005).

5.1.3 Electrophysiology recording of CSD

The phenomenon of CSD was first reported in 1944 by Leão with his observation of silencing of the neuronal electrical activity during ECoG recordings (Leão 1944). Besides, during CSD, cortical neurons covered by the spreading wave cease to respond to electrical or physiological stimulation, and the extracellular potential becomes negative with respect to an indifferent cortical point. The initial negative potential shift is followed by a smaller but more prolonged positive change. The negative potential change during SD recorded has a maximal amplitude of -5 to -15 mV lasting 1 ~ 2 minutes(Leão 1947, 1951). The massive voltage shift is a result of the redistribution of ions in the extracellular space.

5.1.4 MEAs for recording slow potential change

Cortical spreading depression can be characterized by large changes in the direct current (DC) coupled voltage recording. The conventional instrument for detecting CSD electrical responses are glass microelectrodes. Although multi-electrode arrays are more sensitive to AC voltage change than slow shift in DC potential, previous studies suggested that polarizable electrodes may still be used in recording slow potential changes. Data collected by a platinum electrode array suggested that ECoG depressions detected are identical to those found in CSD (Fabricius et al. 2006). Voltage deflection that has similar latency and shape is recorded during anoxia depolarization by a platinum microfabricated multi-electrode array (Thiébaud et al. 1999). The polarizable electrode is expected to record the signals reflecting the AC derivative of the slow potential change instead of the DC change itself.

In this chapter, we report the combination of optical recordings with flexible microelectrode array recordings for brain slice research where we stimulate a brain slice with chemicals injected by the microfluidic ports reported in Ch.2 and study 2D CSD waves. We show evidence that in addition to the high frequency action potential signals, the Au electrode array is able to detect the onset of the CSD DC voltage shift. By monitoring optical recordings and the electrophysiology results simultaneously, we also demonstrate a possible mechanism for cortical spreading convulsion.

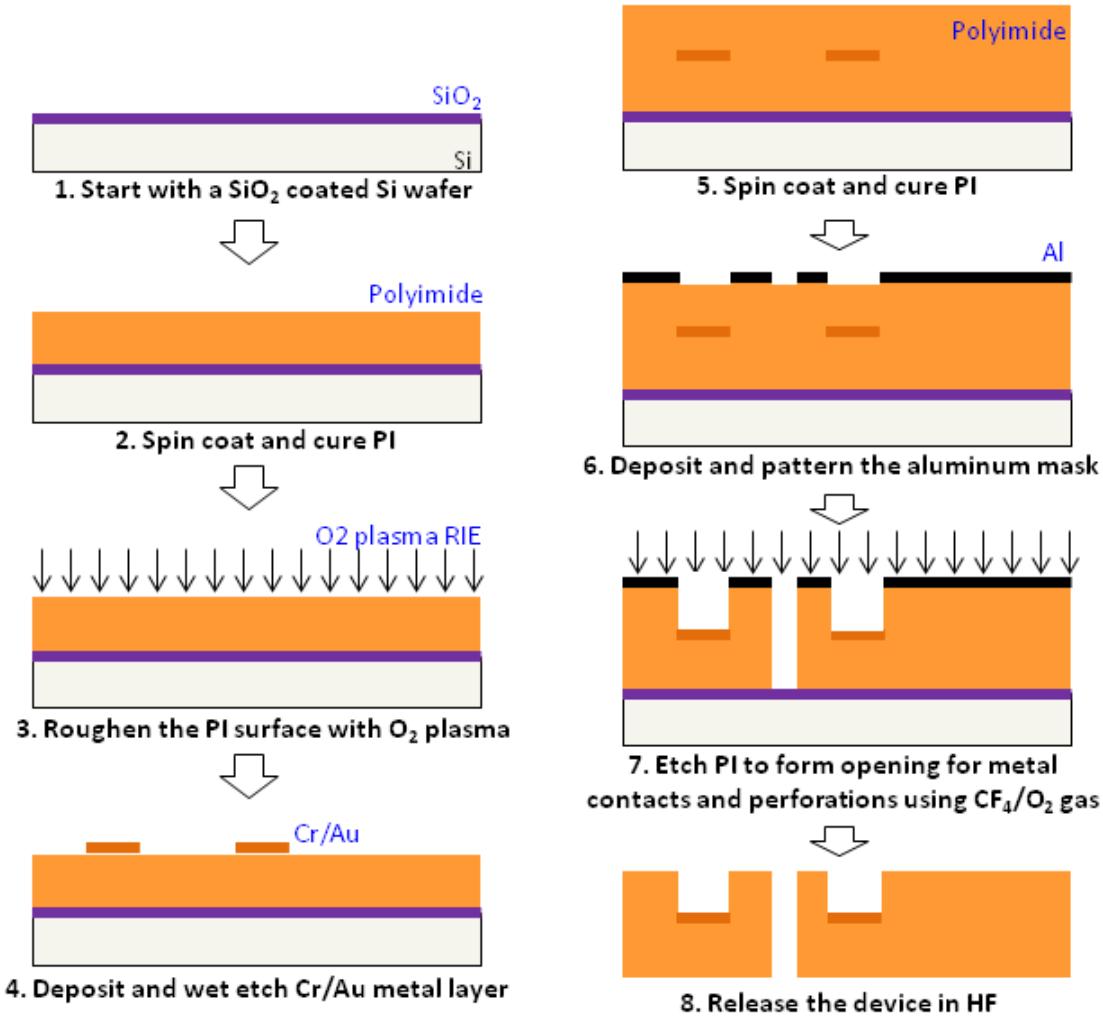

Figure 5.1: Abbreviated process flow for fabricating the flexible multielectrode array

5.2 Methods

5.2.1 Planar Flexible MEA (fMEA) Design and Fabrication

The fabricated electrode array has an effective area of 4.4 mm^2 to cover the cortical area of a brain slice with two basic material components: polyimide and gold. Gold is chosen as the electrode material due to its inert nature. Polyimide, being flexible and transparent, has been a popular insulation material in biocompatible flexible electronics. To record cortical neuronal signals, the electrode array needs to cover the whole thickness of the cortex (1 mm) and follow the curvature of the slice. Each MEA contains 23 gold electrodes which are arranged along three equally spaced lines (spacing: 319 μm; length: 2.294 mm), each parallel to the cortex pial surface in a typical coronal rodent brain slice. Each electrode consists of a round gold pad with a slightly smaller square opening in the polyimide insulation layer serving as an electric interface with the tissue. The opening area of the electrode site is 50 by 50 μm. Perforation holes are placed in between metal interconnects to ensure the supply of ACSF which delivers nutrients and oxygen to the slice. The total area of the perforation holes consists about 17% of the total electrode area in contact with the slice. The thickness of the polyimide layer is determined empirically to be around 5 μm so that the membrane is flexible enough to follow the slice surface morphology and rigid enough to be handled. Thin membrane also assures good transparency which allows high signal-to-noise ratio (SNR) in the imaging. Next, we design the metal traces to ensure intact electrical connectivity in them when the array is bent. Serpentine shaped metal traces have

shown improved bending strength that is suitable for flexible electronics interconnects(Kim et al. 2011). The metal traces connecting the electrode active sites to the contact pads are designed in serpentine shape.

The fabrication process is illustrated in Fig 5.1. The process begins with spin-coating a polyimide (PI) layer (3.4um, PI-2546, , HD MicroSystems, Parlin, NJ, USA) on a silicon wafer with a SiO_2 top layer (1μm) pre-coated by thermal oxidation. The PI layer is cured in an nitrogen-purged oven by ramping up to 350^{o}C for 1.5 hour and holding at 350^{o}C for an additional hour. The PI surface is then roughened by oxygen plasma reactive ion etching. E-beam evaporation, photolithography and wet etching deposit and define the metal traces (Au/Cr 145/5 nm). The rough contour on the bottom PI layer is transferred to the metal layer. The roughened surface has an increased "effective" surface area and this will decrease the final metal electrode impedance as the electrode impedance is reversely proportional to the effective area(Paik et al. 2003). A second PI layer (5μm) is then spun onto the substrate and cured under the same condition as the first PI layer. E-beam evaporated aluminum layer is used as the mask for subsequent dry etching the PI layer to define the perforation holes and electrode sites. The two PI layers are etched through in a gas combination of O_2 and CF_4 (gas flow 15:75 sccm, pressure 100 mTorr, power 200 W) with an etch rate of approximately 0.5 μm/min. The flexible array is released by dipping the wafer in BOE (6:1) until the sacrificial oxide layer is dissolved.

After release, the device is rinsed in DI water and dried on a piece of Si wafer. Anisotropic conductive tape (Elform) is used to connect the contact pads on the MEA to a flexible flat cable which connects to a 24 - channel BNC breakout box. Room temperature cured

silicone (Ecoflex) is applied at the bonding area to provide insulation over the exposed connection. When the device is ready for use, a drop of DI water is applied onto the flexible MEA and the device could be easily peeled off by forceps.

5.2.2 Impedance spectroscopy measurements

The impedance of the released device is measured (HP4284A LCR meter) at frequencies ranging from 200 Hz to 100 KHz against an Ag/AgCl reference electrode dipped in 0.9% physiological saline solution at room temperature. An AC sinusoidal wave of 5mV in amplitude is applied to the electrode and the DC potential is set to 0V.

Impedance of the electrodes are occasionally confirmed prior to brain slice experiment by applying a sinusoidal perturbation voltage of 20 mV to the electrode in physiological saline and measure the signal by the amplifiers. With the input impedance of the amplifier being approximately 1 MΩ, the impedance of the electrode could be derived with an equivalent voltage divider circuit.

5.2.3 Preparation of brain slices

Experimental protocols are approved by the UCLA Chancellor's Animal Research Committee. Mice brain slices were prepared as described in our previous work. Briefly, male C57Bl/6 mice (25 ~ 30 g) were deeply anaesthetized with isoflurane and decapitated. The brain was rapidly removed and immersed in ice-cold high sucrose low sodium artificial cerebrospinal

fluid (ACSF) of the following composition (in mM): 220 sucrose, 3 KCl, 10 $MgSO_4$, 1.25 NaH_2PO_4, 0.2 $CaCl_2$, 25 $NaHCO_3$, 25 D-glucose bubbled with 95% O_2, 5% CO_2. The brain was then glued to a stage and coronal slices of 400 μm thickness were cut in ice cold oxygenated sucrose solution with a standard vibratome (MA752 Motorised Advance Vibroslice, Campden Instruments). The slices were then incubated in an oxygenated ACSF solution (in mM: 125 NaCl, 3 KCl, 1.25 NaH_2PO_4, 1.3 $CaCl_2$, 1.3 $MgSO_4$, 25 $NaHCO_3$, 25 D-glucose) at 32^oC for at least one hour before the experiments.

5.2.4 Stimulation and Solutions

High-K^+ ACSF solutions containing 9, 20, 50, 70, 80 mM of K^+ which replace equimolar Na^+ in normal ACSF are used for CSD induction. The minimum concentration that would induce CSD is 15 mM as measured in previous experiments (Ch. 4). To increase neuron excitability but below CSD induction threshold, ACSF containing 12 mM $[K^+]_e$ in total replaces the normal ACSF for perfusion. CSD is induced by either perfusion of high K ACSF through the local port or bath perfusion. To ensure successful CSD induction, bath perfusion $[K^+]_e$ concentration is selected to be 20 mM which is slightly above the threshold. When applying chemical stimulation with a confined plume with the assembly of injection/suction ports, solutions with 50, 70, 80 mM of $[K^+]_e$ have been used. If CSD fails to initiate, indicating that the plume area and the concentration combination is below threshold, suction is turned off to allow CSD induction with an enlarged plume. If no CSD is recorded for two consecutive injection tests even with the unconfined plumes, the slice is considered inactive and will be replaced. If a slice does exhibit

response, stimulation is allowed to continue with a 10-minute interval between each injection test until responses disappear and the slice is considered no longer viable.

5.2.5 Imaging

The brain slice is imaged using a 2x objective (Carl Zeiss) coupled to a high sensitivity camera (Infinity2, Lumenera Coorporation) mounted above the chamber. Blue LED light (470nm, half width 25nm; Luxeon III, Phillips Lumileds) is directly shed onto the slice and the excited green light was passed through a filter (emission > 515 nm; Chroma Technology) for fluorescence imaging. A green LED (500 ~ 540 nm) directly illuminates the slice for optical intrinsic signal imaging. Images are acquired at 2 Hz; pixel size was 1.59 μm.

During imaging, detection of the fluorescent plume as well as the intrinsic signal changes caused by CSD is realized with alternating fluorescence and reflected light. Lights are powered and controlled by a LED driver (SLA-Series, Mightex Systems) connected to connector block (BNC-2110, National Instruments, Taxes) interfaced with a computer. A custom Labview recording program is written so that one frame of fluorescence image is collected for every 60 frames (30 s) of intrinsic signal. In this way the electrophysiology recording is also synchronized with the imaging.

5.2.6 Electrophysiology Recording

Signals recorded by the electrode array are amplified by two four-channel instrument amplifiers (Brownlee Precision 210A and 440A). Eight channels are selected for recording during each experiment based on the electrode locations on slice. Each channel is AC coupled and magnified 200 times (0.01 Hz highpass filtered and 3000 Hz lowpass filtered). Equipment settings for both amplifiers are identical except that the model 440A has an added in-line notch filter which removes the 60 Hz line noise. Data are collected by a data acquisition card (BNC-2110, National Instruments,) and a custom Labview program. Sampling frequency is 1000 Hz for slow potential waves and 10000 Hz for evoked epileptiform bursts. Offline data processing is performed with a custom Matlab program. An Ag/AgCl wire is inserted in the chamber solution serving as the ground.

5.2.7 Experiment procedure

The electrode is let floating in the brain slice chamber before loading the slice into the chamber. After the slice is positioned on the port, a metal ring with nylon wire mesh is used to push the electrode into the solution and position it so that the electrode array is on the cortex. The slice, electrodes and the nylon mesh are submerged in solution throughout the experiment. Suction is kept on all the time. Injection is turned on right before recording starts and turned off when CSD is induced or imaging is finished, whichever is earlier.

5.2.8 Data Analysis

Traces are digitally notch (60 Hz and harmonics) and low-pass (0.05 Hz) filtered. We noticed there is a small DC drift (0.1 ~ 10 mV in 300 s) and therefore the baseline is subtracted from the filtered signal to better visualized the voltage change. CSD wave arrival time is determined as the time that minimum slope occurs on the curve for the voltage to reach its negative maximum. In OIS recordings, the wave arrival time is determined as the time when the wave spreads to the center of the electrode site. Noise is measured before some of the experiment with the same condition as recording.

5.3 Results

5.3.1 Properties of the electrode

5.3.1.1 Flexibility

To evaluate the bending performance as an indication of flexibility of the electrode array, a droplet of deionized water is added to the electrode array and by surface tension, the electrode array folds by itself and the electrodes part sticks to the interconnect part. Fig 5.2 (A, B) shows the folded electrode array with a minimum bending radius around 260 μm. Once the water is dried by a piece of paper, the electrode array is released and returns to its original flat shape. The electrodes show no difference before and after bending morphologically and electrically (data not shown).

5.3.1.2 Transparency

Fig 5.2 (C) illustrates the electrode array positioned above a functioning fluidic port, promising a practical transparency level for application in an upright microscope setup.

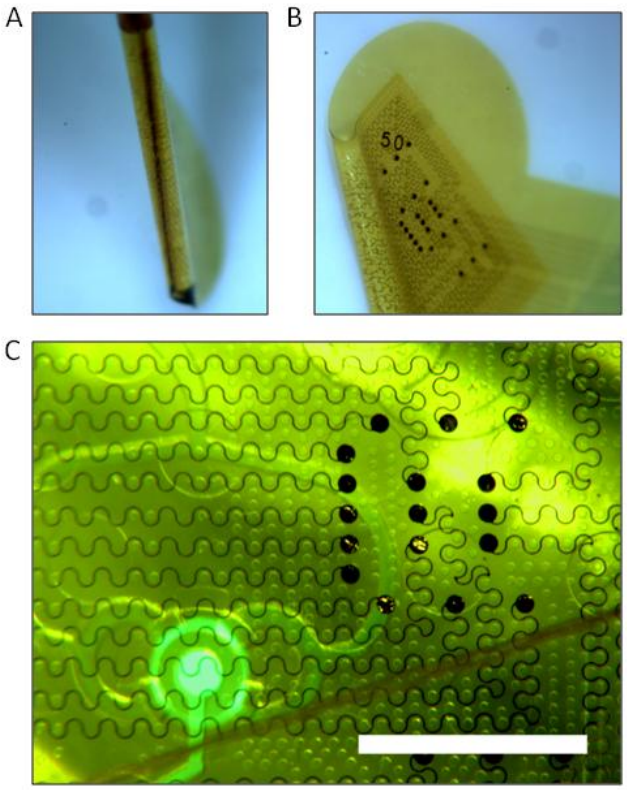

Figure 5.2: The flexible and transparent MEA.

Images of folded electrode array around a drop of DI water. (A) Side view. (B) Front view. (C) MEA on top of the fluid port. The fluorescent plume injected by the device is clearly visible. Bar 1mm

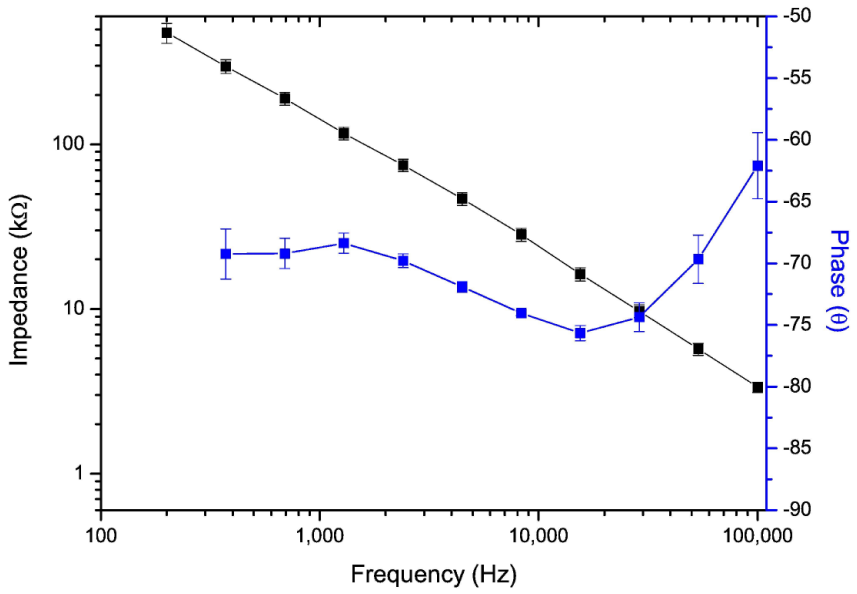

Figure 5.3: Interface impedances of microelectrodes with frequency ranging from 200 Hz to 100 kHz. At 1 kHz, the impedance is 102kΩ.

5.3.2 Performance of the electrode

5.3.2.1 Impedance spectroscopy

The electrical properties of the 23 different electrodes in the array were measured using an impedance analyzer. In Fig 5.3, the electrode-electrolyte interface impedance of 8 electrodes has an average magnitude of 102 kΩ at 1 kHz for an electrode opening area of about 50 x 50 μm^2. A linear relationship between log f and log |Z| is observed. The phase at 1 kHz for the gold microelectrode is -69^o. The phase change is small in the testing frequency range (González and Rodríguez 1997). Noise level for the electrode array is 10 ± 8 μV.

5.3.2.2 Influence to the viability of the slice

To test the viability of slices covered by the electrode array, we stimulate slices with localized/leaky plumes in the same cortical area until CSD could no longer be induced. Slices are active for at least 3 hours with 11 CSD waves induced at the same induction site, comparable to those without electrode arrays placed on top. Also, no spontaneous SD-like waves induced by hypoxia are observed (Somjen 2001). This confirmed that the nutrient and oxygen supply is not appreciably restricted with the polyimide electrode array with perforation holes.

5.3.3 Electrophysiology

5.3.3.1 Experiment setup

The experimental setup we use to characterize our devices and perform CSD induction experiments is shown in Fig. 5.4. The setup is housed in a Faraday cage which sits on a floating table. The BNC breakout box which connects the device with flat ribbon cable is secured and the only movable part is the lower part of ribbon cable and the electrode array. The electrode array is placed into the perfusion chamber from above and let float on the perfusion fluid before the experiment. When pushed under the ACSF surface, the electrode array stays still and don't move unless big fluctuation in the perfusion chamber occurs. The movement disturbance to the electrophysiology recording is differentiable from CSD signal (discussed below).

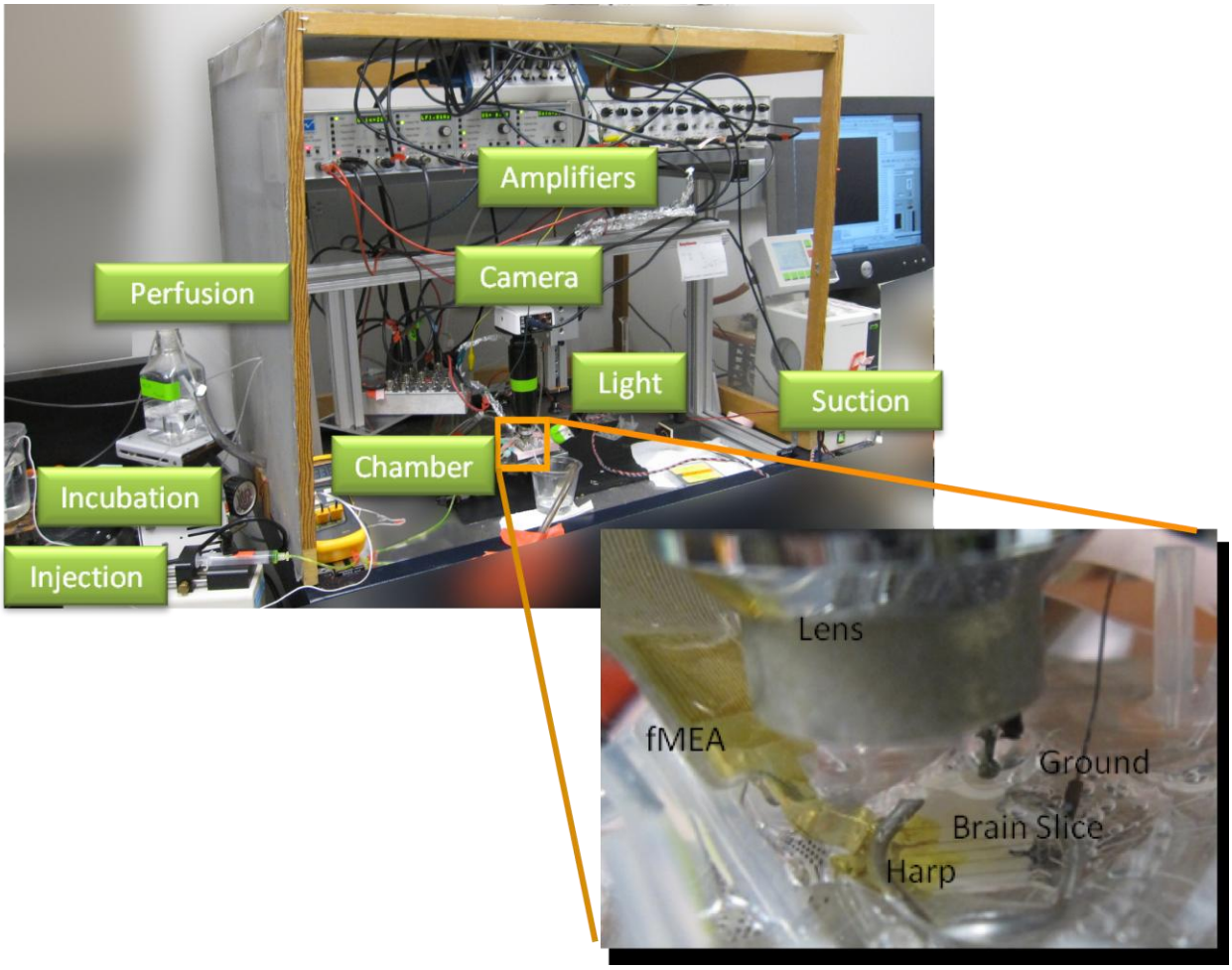

Figure 5.4: Experiment setup for both microfluidic device and fMEA.

Enlarged inset show the concurrent use of fMEA and the brain slice chamber

5.3.3.2 Spontaneous activity

Spontaneous activities are sometimes recorded by the electrodes. Action potentials could be recorded before and after CSD occurs.

5.3.3.3 Evoked activity

High $[k^+]_e$ in the bathing ACSF solution increases the neuronal excitability and induces epileptiform bursting in the cortex (Schweitzer et al. 1992; Jensen and Yaari 1997) The bursts in the slices are characterized by high-frequency spikes followed by a suddenly disappearance of activities. Fig 5.5 shows the epileptiform bursting recorded by one electrode. The spikes persists for more than 300 s with the single spike amplitude being 20 ~ 40 mV with 2 ms duration.

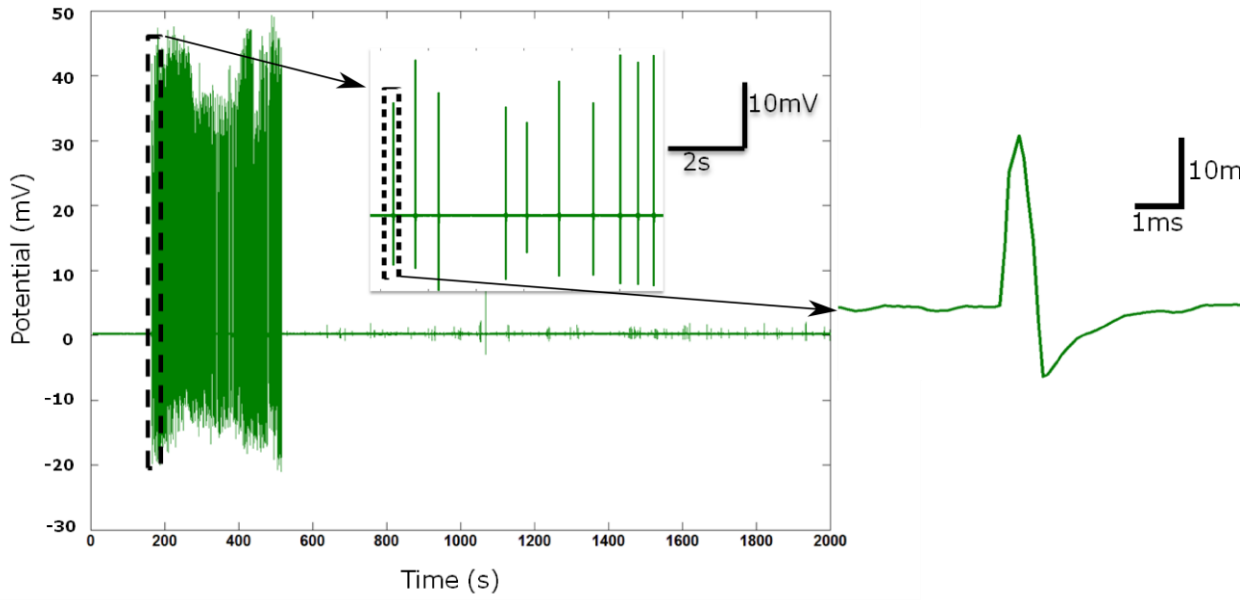

Figure 5.5: Spontaneous and Evoked Activity.

Inset shows enlarged electrophysiology recordings of the epileptiform bursting. A single spike is shown on the right panel.

5.3.3.4 CSD response

CSD is characterized by a DC slow potential change lasting around 1 ~ 3 minutes. Although the lower frequency limit of the amplifier's AC filtration is 0.01 Hz, frequencies lower than that is detectable in the recorded signal (probably with attenuation). Due to the derivative transformation function of the AC-coupled amplification, this DC shift is reflected in the recorded signal as a voltage deviation from the baseline level predominantly in the negative direction at the starting point of the DC shift(Fabricius et al. 2006). The negative voltage shift has two forms: a transient peak during which the potential returns to the original baseline in a similar rate as it drops to its minimum; a similar voltage drop but with a much slower return from the negative peak. Mechanisms accounting for the difference in the recovery time are not clear with the available data. In almost all cases, the small voltage deviation is distinguishable in the raw waveform data. The purpose of the low pass filtering is only to better visualize the signal. The onset time of the voltage deviation indicating the passage of a CSD wave coincides with the appearance of OIS signal at that recording site.

Fig 5.6B shows signal recorded by a glass micropipette and three electrodes from the array that are closest to the pipette. Negative voltage deflections are observed in the microelectrode recordings. The glass microelectrode shows a DC potential shift in the negative direction at a similar time as electrode no. 2 and 3. Differences in the onset time for the negative shift in the baseline change indicate a propagation wave, which is consistent with the intrinsic optical signal showing in Fig 5.6A. The magnitudes for two recording differ as the glass

electrode records the true DC shift while the gold microelectrode array records the AC-derivative of the DC shift.

Fig 5.7B shows typical negative voltage deviations from baseline recorded after CSD is induced by a localized injection, with a delay between onsets of voltage changes at different electrodes, showing evidence of a CSD wave spreading over the area covered by the electrode array. The onset of the voltage shift that occurs when high-K^+ ACSF solution is perfused through the injection port and successfully induces CSD coincides with the time of the CSD wave passing the electrode extracted from OIS recording (Fig 5.7A).

To rule out the artifacts caused by local slice movements induced by chemical injection, we perfuse the whole slice with elevated $[k^+]_e$ ACSF to induce CSD. In Fig 5.8 we show data from a slice perfused with 20 mM $[k^+]_e$ ACSF. Identical negative potential changes are recorded in most of the electrodes with finite delays between each other. This shows that local slice movement doesn't account for this negative voltage shift. As voltage changes due to movement occur at the same time on all electrodes, the caused artifact can therefore be differentiated with CSD signals.

The mean voltage deflection level is 3.0 ± 2.6 μV (n=172, mean ± SD, 25 percentile: 1.4, 75 percentile: 3.5, unit: μV). Among all the experiments, 149 measured voltage change occurrence are within 10 s to the wave arrival at the electrode from optical recordings. The average time difference is 2.6 ± 2.3 s (mean ± SD). Since the voltage shift always closely agrees with the appearance of optical signals at the recording electrode, we conclude that the voltage changed recorded by the polarizable electrodes are indication of the passage of CSD waves.

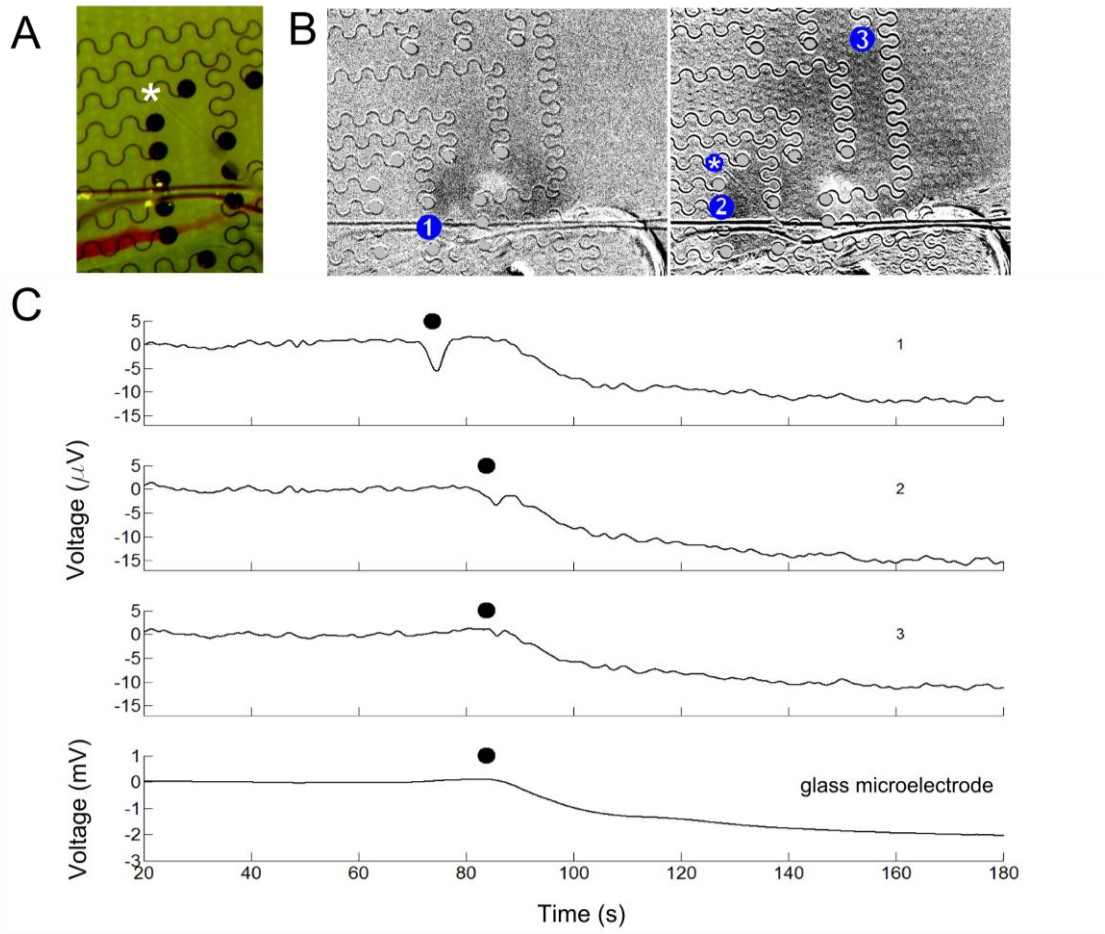

Figure 5.6: Glass micropipette electrophysiological signal coincides with fMEA signal.

(A) Image shows the fMEA on top of the brain slice with the glass pipette tip (white star) piercing through one perforation of the membrane into the brain slice. (B) Optical recordings of the CSD wave passing the cortex covered by a flexible MEA. Wave front is seen as the darkened area. White star in the left panel marks the glass microelectrode location. (C) Electrical potential recorded by the flexible MEA (black traces 1~3) and a glass microelectrode (lowest trace). Black filled circles show wave arrival time in (B) at each electrode.

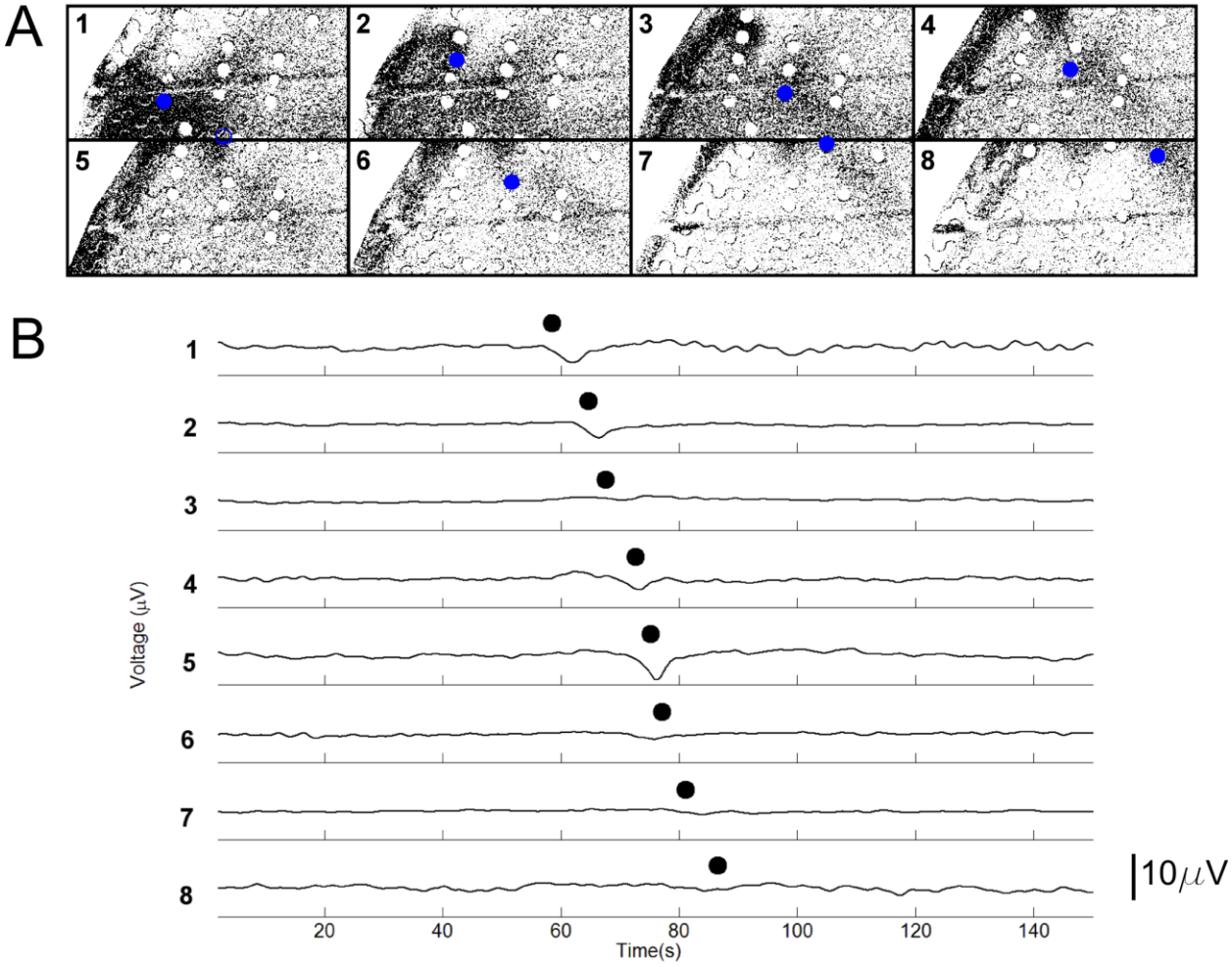

Figure 5.7: Slow DC Change accompanying CSD initiated by a localized high-K^+ plume.

(A) Optical recordings of the CSD wave passing the cortex covered by a flexible MEA. Wave fronts are shown as the darkened area. Wave direction: lower left to upper right. Filled blue circles indicated the recording electrodes location. Note, electrode #5 has only the lower half the area included in the field of view. (B) Electrical potential recorded by the flexible MEA (black traces). Black filled circles show wave arrival time in (A) at each electrode. Except for electrode #8, voltage deflection (amplitude ranges from 0.7 ~5.5 μV) are consistent with optical signals. Full range: -5 ~ 5μV.

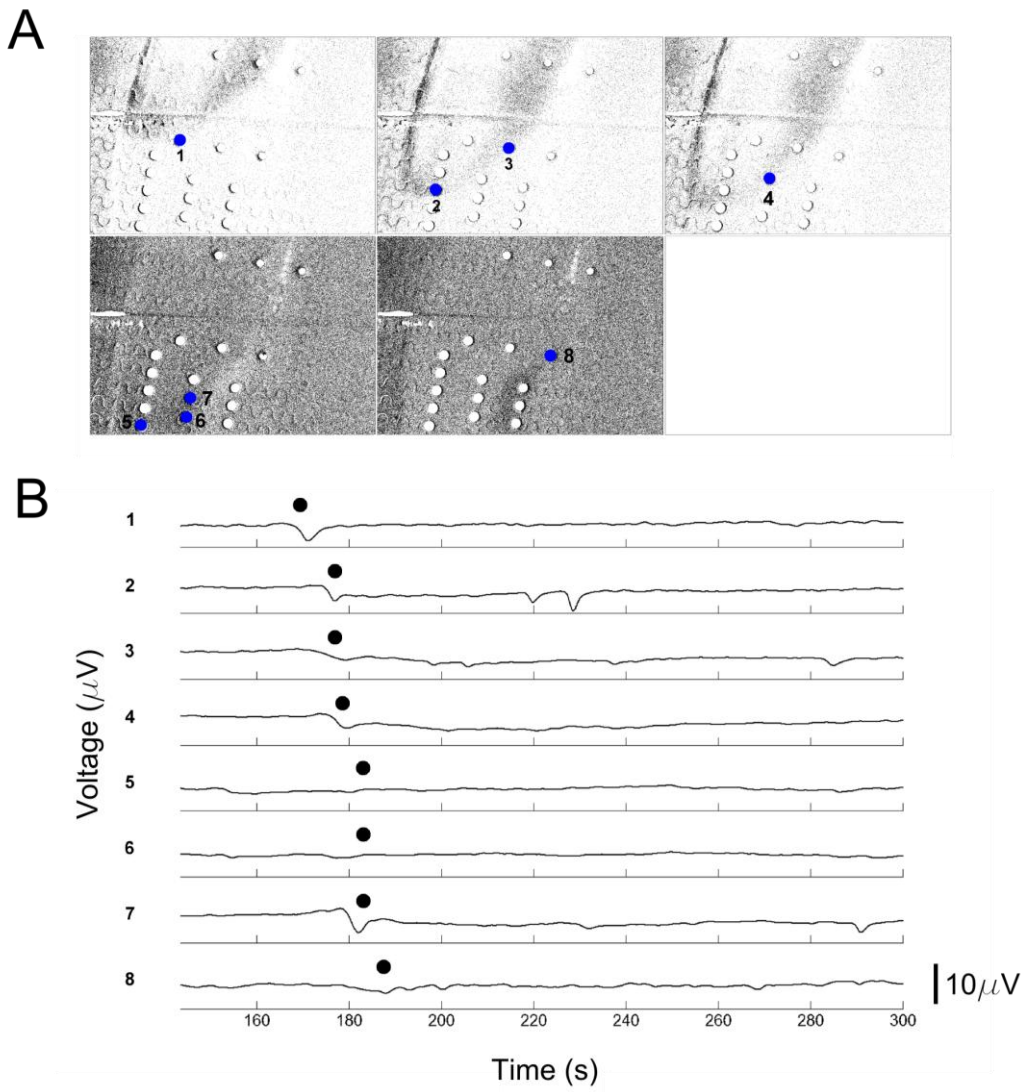

Figure 5.8: Slow DC Change of CSD initiated by bath perfusion of high-K^+ ACSF solution.

(A) Optical recordings of the CSD wave passing the cortex covered by a flexible MEA. Wave fronts are shown as the darkened area. Wave direction: downwards. Filled blue circles indicated the recording electrodes location. (B) Electrical potential recorded by the flexible MEA (black traces). Black filled circles show wave arrival time in (A) at each electrode. Except for electrode #5,6 and 8, voltage deflection (amplitude ranges from 0.8 ~5.0 μV) are consistent with optical signals. Full range: -5 ~ 5mV.

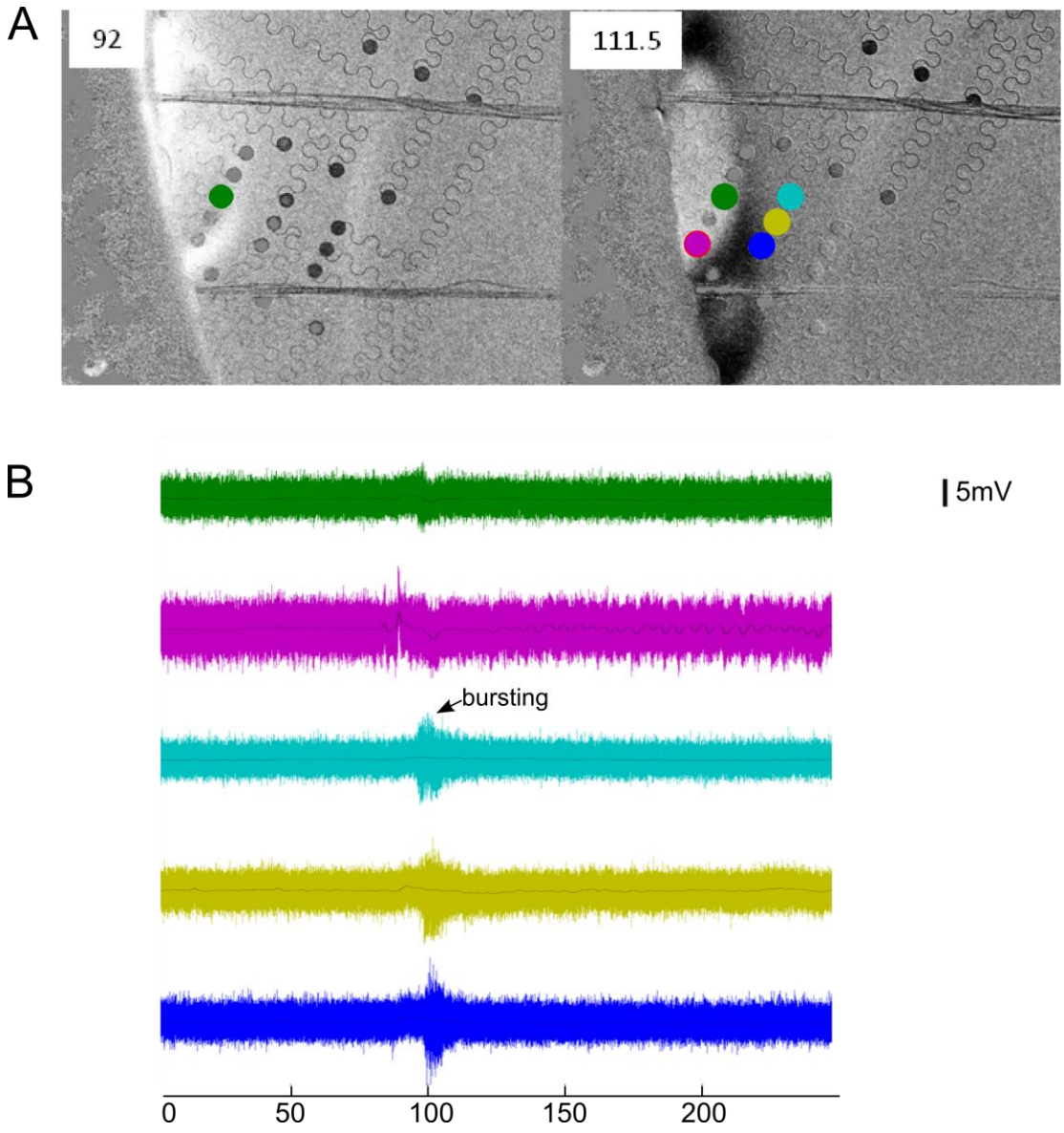

Figure 5.9: Different electrical responses at the wave boundary.

(A) CSD wave propagation confined in the upper cortical layers. Wave fronts are shown as the darkened area. Wave arrives at the green electrode at 92s (left) and passes all recording electrodes at 111.5s (right). (B) Electrical recordings show voltage deflection in the first two traces and bursting in the lower three traces whose corresponding electrodes lie on the border of CSD wave propagation area and the inert tissue.

In two of the experiments where we observe wave spreading only in the superficial layers, we have several electrodes lie on the border of the superficial cortical area that has CSD spreading over and the area with no indication of wave propagation from OIS recording. Recordings from electrodes in the spreading region and on the border are shown in Fig 5.9. Both voltage shift and epileptiform discharges are observed on three electrodes on the border. This phenomenon is similar to observation reported as "spreading convulsion" where high frequency ECoG spikes are observed during the final shoulder of the negative voltage shift (Dreier et al. 2012).

5.4 Discussion

5.4.1 Polarizable electrode for recording CSD

The phased onset of potential deflection among different electrodes that we observe in a number of instances and slices, with the onset time coincides with the characteristic optical intrinsic signals of CSD, is compelling evidence that CSD is the correlation of the observations in our study. The data presented here provide definite evidence that polarizable electrodes can be used to record near DC slow potential change (i.e. CSD wave).

The noise level for the electrode (V_{rms}) is 10 ± 8 μV. Signal level of the voltage deviation is 3.0 ± 2.6 μV. Amplitude of a single spike in the epileptiform bursting recording is 30 to 60 mV. So the SNR is less than 1 for most cases in near DC recordings and larger than 3000 for high frequency recordings. Although the SNR is small for the signal we are mostly interested in,

the CSD signal detected is regarded as valid for two reasons: 1) Noise mostly appears in a frequency that is much faster than the DC deviation frequency, so low frequency filtering is effective in extracting the slow potential change 2) Voltage deflection can always be confirmed by referencing the optical recordings.

The impedance spectroscopy results show that the electrode impedance decreases as frequency increases. The impedance of the electrode at near DC frequency is higher than the input impedance of the amplifiers. Under this situation, signal is attenuated by the ratio of two impedance values (electrode and amplifier's input impedance) approximately. At higher frequencies, the signal will be preserved as the electrode impedance is much lower. The influence of electrode impedance on signal amplitude is confirmed by our results showing that nearly 5000 times higher signal amplitude of the epileptiform bursting (around 1 kHz) than CSD wave (near DC) is observed. Improvement on lowering the impedance of the electrodes would further enhance the SNR at near DC recordings.

5.4.2 Cortical Spreading Convulsion (CSC)

Cortical spreading depression is characterized by a sustained depolarization happens in the cortex which remains above the inactivation threshold of action potentials. The depolarization eventually causes the brain to enter a depression state and the recovery to the normal state shows a delay in the recovery of inhibitory interneurons compared to the excitatory neurons(Somjen 2001). Therefore, at the recovery period of the spreading depression, there are less inhibitory interneurons and this might facilitate the occurrence of epileptiform bursting at

this period. Still, the mechanism underlying spreading convulsion is not completely understood. Results in Van Harreveld and Stamm's work suggest that vasodialation (failure of vasoconstriction) will contribute to the gradual transition from CSD into CSC after a series of stimulation(Van Harreveld and Stamm 1954). The actual occurrence of cortical spreading convulsion might coincide with the unphysiological conditions of the tissue(Dreier et al. 2012). When correlating the electrophysiology recording data in synchronization with the optical wave propagation pattern, we find that the epileptiform burst discharge only occurs at the boundary of cortical regions with and without CSD wave propagation. The regions that are not capable of supporting CSD wave propagation might suggest inactive/metabolically failed neurons. In the cortical area that show convulsive pattern, wave propagation is not observed optically in the following 4 ~ 6 stimulations (1 ~ 1.5 hr experiment time) suggesting no recovery.

5.4.3 Significance

Although Ag/AgCl wire based multielectrode array has been proposed with the potential to record near DC voltage change (Scott et al. 2012), the conventional platinum or gold based multielectrode array still has advantages. First of all, the fabrication processes and integration capability of Pt/Au based MEA are well developed whereas the fabrication of reliable Ag electrodes remains challenging. Due to the notable consumption of Ag^+ ions during the recording, and the fact that the microfabricated Ag membrane thickness is limited (< 100s μm), Ag electrodes need a replenishing mechanism for reliable long-term operations. Secondly,

electrodes used in human research and diagnosis are mostly noble metal based and Ag/AgCl wires are considered neurotoxic or hazardous (Cooper and Crow 1966). Polarizable electrodes in brain slice experiments, therefore, offers closely resembled results to their *in vivo* counterparts.

5.5 Summary

A flexible multi-electrode array is demonstrated with the ability to record extracellular DC potential change that coincides with changes in the intrinsic optical signal. This indicates CSD can be studied with a 2D electrode array for improved spatial resolution. By analyzing the electrical recording simultaneously with optical images, novel information regarding cortical spreading convulsion is discovered.

CHAPTER 6 Conclusion

This work demonstrates the implementation of microfabricated devices in brain slice study. With the new devices, we are able to broaden our knowledge of the brain and interpret neuronal phenomenon with a more comprehensive perspective. Including our work, the development in brain slice study tools based on micro-technology has been more and more learned and appreciated in the neuroscience field. This is mainly due to the fact that not only technical breakthroughs, but also the sprouting biologically meaningful results have been shown with the new technology.

Ongoing researches focus on several compelling challenges: (1) Better spatial control over the interstitial flow. Microfluidics techniques have been implemented for controlling the flow around/outside the brain slice. The critical mass being affected inside the slice is not directly controlled by the devices, but by extracellular diffusion, mostly. Therefore, an intriguing tool for chemical stimulation would have the capability to better control the substance distribution inside the slice. (2) Higher signal to noise ratio for electrical recordings. The surface dead cell layer and the intrinsically less electrical activity of the slice dramatically reduce the signal strength detected by surface electrode array. The marriage of flexible electronics and 3D low impedance electrodes would be a promising tool for a brain slice chamber add-on. (3) Single cell targeting techniques. Patch clamp recording from cells and loading drugs to the intercellular space are all valuable techniques to study the neuronal activities in the cellular, synaptic and network levels. Microfabricated brain slice chambers integrated with the cellular level study functionalities will be valuable and attractive to neurophysiologists.

There are, however, still limitations lie in these novel devices that need to be overcome. Firstly, due to the hydrophobicity of PDMS, a popular microfluidic device material, bubbles cause a prevalent issue for the device performance. Bubbles are easily trapped in small channels or at defects due to fabrication imperfection. These bubbles disrupt the controlled condition and compromise the experiment accuracy. At biological relevant temperatures that are usually required for brain slice study (32~36^{o}C), the appearance of bubbles is even more severe. Secondly, small channels in tissue study are prone to clog by tissue fragments. The biological solutions also will crystallize inside the channels and worsen the clog. Therefore, microfluidic devices require careful cleaning after each usage. Improper cleaning will deteriorate the device performance. Compare to the disposable glass micro pipette, this is a serious drawback as it could cost much more to use a microfabricated device due to unfamiliar handling. Thereby, decreasing the device cost and improve the chemical resistance of the device material is desirable.

Microfabricated devices for brain slice study present a promising tool to facilitate the advance in neuroscience research. As the majority of users intended for these tools remains the neuroscientists, rather than the engineers who design the tools, filling the gap between the traditional tools and the innovative devices are vital. To be an alternative for traditional tools, microfabricated devices need to be easy to handle, conceptually straightforward, flexible for meeting different application needs and adaptable to the same equipments (pumps, amplifier, etc) in the neurology labs. This requires a close collaboration between engineers and biologists, for the neuroscientists to appreciate the advantages of novel tools over the tried-and-true methods and for the engineers to design devices that not only overcome the engineering challenge but also are useful and practical to neuroscientists.

REFERENCES

Ainla A, Jansson ET, Stepanyants N, Orwar O, Jesorka A. 2010. A microfluidic pipette for single-cell pharmacology. Analytical chemistry. 82:4529–4536.

Ainla A, Jeffries GDM, Brune R, Orwar O, Jesorka A. 2012. A multifunctional pipette. Lab on a chip. 12:1255–1261.

Aitken PG, Tombaugh GC, Turner DA, Somjen GG. 1998. Similar propagation of SD and hypoxic SD-like depolarization in rat hippocampus recorded optically and electrically. Journal of neurophysiology. 80:1514–1521.

Arai F, Ichikawa a, Ogawa M, Fukuda T, Horio K, Itoigawa K. 2001. High-speed separation system of randomly suspended single living cells by laser trap and dielectrophoresis. Electrophoresis. 22:283–288.

Armstrong GAB, Rodgers CI, Money TGA, Robertson RM. 2009. Suppression of spreading depression-like events in locusts by inhibition of the NO/cGMP/PKG pathway. The Journal of neuroscience : the official journal of the Society for Neuroscience. 29:8225–8235.

Ayata C, Jin H, Kudo C, Dalkara T, Moskowitz MA. 2006. Suppression of cortical spreading depression in migraine prophylaxis. Annals of neurology. 59:652–661.

Bancroft JD, Gamble M. 2008. Theory and Practice of Histological Techniques. 6th ed. elsevier health Sciences.

Binder DK, Papadopoulos MC, Haggie PM, Verkman a S. 2004. In vivo measurement of brain extracellular space diffusion by cortical surface photobleaching. The Journal of neuroscience : the official journal of the Society for Neuroscience. 24:8049–8056.

Blake AJ, Pearce TM, Rao NS, Johnson SM, Williams JC. 2007. Multilayer PDMS microfluidic chamber for controlling brain slice microenvironment. Lab on a chip. 7:842–849.

Blau a W, Ziegler CM. 2001. Prototype of a novel autonomous perfusion chamber for long-term culturing and in situ investigation of various cell types. Journal of biochemical and biophysical methods. 50:15–27.

Blau A. n.d. Prospects for Neuroprosthetics: Flexible Microelectrode Arrays with Polymer Conductors.

Boppart S a, Wheeler BC, Wallace CS. 1992. A flexible perforated microelectrode array for extended neural recordings. IEEE transactions on bio-medical engineering. 39:37–42.

Bowyer SM, Aurora KS, Moran JE, Tepley N, Welch KM. 2001. Magnetoencephalographic fields from patients with spontaneous and induced migraine aura. Annals of neurology. 50:582–587.

Brennan KC, Romero Reyes M, López-Valdés HE, Arnold AP, Charles AC. 2007. Reduced threshold for cortical spreading depression in female mice. Annals of neurology. 61:603–606.

Cao Y, Welch KM, Aurora S, Vikingstad EM. 1999. Functional MRI-BOLD of visually triggered headache in patients with migraine. Archives of neurology. 56:548–554.

Chang JC, Brewer GJ, Wheeler BC. 2006. Neuronal network structuring induces greater neuronal activity through enhanced astroglial development. Journal of neural engineering. 3:217–226.

Charles AC, Brennan KC. 2009. Cortical spreading depression-new insights and persistent questions. Cephalalgia : an international journal of headache. 29:1115–1124.

Cheung KC. 2007. Implantable microscale neural interfaces. Biomedical microdevices. 9:923–938.

Choi Y, McClain M a, LaPlaca MC, Frazier a B, Allen MG. 2007. Three dimensional MEMS microfluidic perfusion system for thick brain slice cultures. Biomedical microdevices. 9:7–13.

Christ KV, Turner KT. 2011. Design of hydrodynamically confined microfluidics: controlling flow envelope and pressure. Lab on a chip. 11:1491–1501.

Croning MD, Haddad GG. 1998. Comparison of brain slice chamber designs for investigations of oxygen deprivation in vitro. Journal of neuroscience methods. 81:103–111.

Cullen DK, Vukasinovic J, Glezer A, Laplaca MC. 2007. Microfluidic engineered high cell density three-dimensional neural cultures. Journal of neural engineering. 4:159–172.

Dahlem MA, Hadjikhani N. 2009. Migraine aura: retracting particle-like waves in weakly susceptible cortex. PloS one. 4:e5007.

Davis MJ, Gore RW. 1987. Double-barrel pipette system for microinjection. The American journal of physiology. 253:H965–7.

Dingledine R, Dodd J, Kelly JS. 1980. The in vitro brain slice as a useful neurophysiological preparation for intracellular recording. Journal of Neuroscience Methods. 2:323–362.

Dreier JP, Major S, Pannek H-W, Woitzik J, Scheel M, Wiesenthal D, Martus P, Winkler MKL, Hartings JA, Fabricius M, Speckmann E-J, Gorji A. 2012. Spreading convulsions, spreading depolarization and epileptogenesis in human cerebral cortex. Brain : a journal of neurology. 135:259–275.

Edelman GM, Mountcastle VB. 1982. The Mindful Brain: Cortical Organization and the Group-Selective Theory of Higher Brain Function. The MIT Press.

Fabricius M, Fuhr S, Bhatia R, Boutelle M, Hashemi P, Strong AJ, Lauritzen M. 2006. Cortical spreading depression and peri-infarct depolarization in acutely injured human cerebral cortex. Brain : a journal of neurology. 129:778–790.

Feinerman O, Moses E. 2003. A picoliter “fountain-pen” using co-axial dual pipettes. Journal of Neuroscience Methods. 127:75–84.

Freshney RI. 2005. Culture of Animal Cells: A Manual of Basic Techniques. 5th ed. New York: Wiley-Liss.

Gholmieh G, Soussou W, Han M, Ahuja A, Hsiao M-C, Song D, Tanguay AR, Berger TW. 2006. Custom-designed high-density conformal planar multielectrode arrays for brain slice electrophysiology. Journal of neuroscience methods. 152:116–129.

González C, Rodríguez M. 1997. A flexible perforated microelectrode array probe for action potential recording in nerve and muscle tissues. Journal of Neuroscience Methods. 72:189–195.

Hadjikhani N, Sanchez Del Rio M, Wu O, Schwartz D, Bakker D, Fischl B, Kwong KK, Cutrer FM, Rosen BR, Tootell RB, Sorensen AG, Moskowitz MA. 2001. Mechanisms of migraine aura revealed by functional MRI in human visual cortex. Proceedings of the National Academy of Sciences of the United States of America. 98:4687–4692.

Heinemann U. 1986. Excitatory amino acids and epilepsy-induced changes in extracellular space size. Advances in experimental medicine and biology. 203:449–460.

Heinemann U, Lux HD. 1977. Ceiling of stimulus induced rises in extracellular potassium concentration in the cerebral cortex of cat. Brain research. 120:231–249.

Heinemann U, Lux HD, Gutnick MJ. 1977. Extracellular free calcium and potassium during paroxsmal activity in the cerebral cortex of the cat. Experimental brain research Experimentelle Hirnforschung Expérimentation cérébrale. 27:237–243.

Helmchen F, Denk W. 2005. Deep tissue two-photon microscopy. Nature methods. 2:932–940.

Heuschkel MO, Fejtl M, Raggenbass M, Bertrand D, Renaud P. 2002. A three-dimensional multi-electrode array for multi-site stimulation and recording in acute brain slices. Journal of neuroscience methods. 114:135–148.

Heuschkel MO, Guérin L, Buisson B, Bertrand D, Renaud P. 1998. Buried microchannels in photopolymer for delivering of solutions to neurons in a network. Sensors and Actuators B: Chemical. 48:356–361.

Hill MRH, Greenfield SA. 2011. The membrane chamber: a new type of in vitro recording chamber. Journal of neuroscience methods. 195:15–23.

Holthoff K, Witte OW. 2000. Directed spatial potassium Redistribution in Rat Neocortex. GLIA. 29:288–292.

Hung PJ, Lee PJ, Sabounchi P, Aghdam N, Lin R, Lee LP. 2005. A novel high aspect ratio microfluidic design to provide a stable and uniform microenvironment for cell growth in a high throughput mammalian cell culture array. Lab on a chip. 5:44–48.

Jensen MS, Yaari Y. 1997. Role of Intrinsic Burst Firing, Potassium Accumulation, and Electrical Coupling in the Elevated Potassium Model of Hippocampal Epilepsy. J Neurophysiol. 77:1224–1233.

Kaigala GV, Lovchik RD, Drechsler U, Delamarche E. 2011. A vertical microfluidic probe. Langmuir : the ACS journal of surfaces and colloids. 27:5686–5693.

Kasser RJ, Renner KJ, Feng J-X, Brazell MP, Adams RN. 1988. Spreading depression induced by 100 mM KCl in caudate is blocked by local anesthesia of the substantia nigra. Brain Research. 475:333–344.

Khan AM, Ponzio TA, Sanchez-Watts G, Stanley BG, Hatton GI, Watts AG. 2007. Catecholaminergic control of mitogen-activated protein kinase signaling in paraventricular neuroendocrine neurons in vivo and in vitro: a proposed role during glycemic challenges. The Journal of neuroscience : the official journal of the Society for Neuroscience. 27:7344–7360.

Kim D-H, Lu N, Ma R, Kim Y-S, Kim R-H, Wang S, Wu J, Won SM, Tao H, Islam A, Yu KJ, Kim T -i., Chowdhury R, Ying M, Xu L, Li M, Chung H-J, Keum H, McCormick M, Liu P, Zhang Y-W, Omenetto FG, Huang Y, Coleman T, Rogers JA. 2011. Epidermal Electronics. Science. 333:838–843.

Knot HJ, Zimmermann PA, Nelson MT. 1996. Extracellular K(+)-induced hyperpolarizations and dilatations of rat coronary and cerebral arteries involve inward rectifier K(+) channels. The Journal of physiology. 492.2:419–430.

Kottegoda S, Shaik I, Shippy S a. 2002. Demonstration of low flow push-pull perfusion. Journal of neuroscience methods. 121:93–101.

Kraig RP, Nicholson C. 1978. EXTRACELLULAR IONIC VARIATIONS During SPREADING DEPRESSION. Neuroscience. 3:1045–1059.

Largo C, Cuevas P, Somjen GG, Martin del Rio R, Herreras O. 1996. The Effect of Depressing Glial Function in Rat Brain ln Situ on Ion Synaptic Transmission , and Neuron Survival. Journal of Neuroscience. 16:12219–1229.

Lauritzen M, Dreier JP, Fabricius M, Hartings JA, Graf R, Strong AJ. 2011. Clinical relevance of cortical spreading depression in neurological disorders: migraine, malignant stroke, subarachnoid and intracranial hemorrhage, and traumatic brain injury. Journal of cerebral blood flow and metabolism : official journal of the International Society of Cerebral Blood Flow and Metabolism. 31:17–35.

Lee K-K, He J, Singh A, Massia S, Ehteshami G, Kim B, Raupp G. 2004. Polyimide-based intracortical neural implant with improved structural stiffness. Journal of Micromechanics and Microengineering. 14:32–37.

Leão AAP. 1944. SPREADING DEPRESSION OF ACTIVITY IN THE CEREBRAL CORTEX. J Neurophysiol. 7:359–390.

Leão AAP. 1947. Further observations on the spreading depression of activity in the cerebral cortex. Journal of neurophysiology. 10:409–414.

Leão AAP. 1951. The slow voltage variation of cortical spreading depression of activity. Electroencephalography and clinical neurophysiology. 3:315–321.

Ling G, Gerard RW. 1949. The normal membrane potential of frog sartorius fibers. Journal of Cellular and Comparative Physiology. 34:383–396.

Lossi L, Alasia S, Salio C, Merighi A. 2009. Cell death and proliferation in acute slices and organotypic cultures of mammalian CNS. Progress in neurobiology. 88:221–245.

Lovchik RD, Drechsler U, Delamarche E. 2009. Multilayered microfluidic probe heads. Journal of Micromechanics and Microengineering. 19:115006.

MacAulay N, Zeuthen T. 2012. Glial K(+) Clearance and Cell Swelling: Key Roles for Cotransporters and Pumps. Neurochemical research.

Marshall WH. 1959. Spreading cortical depression of Leão. Physiological reviews. 39:239.

Matsuura T, Bureš J. 1971. The minimum volume of depolarized neural tissue required for triggering cortical spreading depression in rat. Experimental brain research Experimentelle Hirnforschung Expérimentation cérébrale. 12:238–249.

Millet LJ, Stewart ME, Sweedler JV, Nuzzo RG, Gillette MU. 2007. Microfluidic devices for culturing primary mammalian neurons at low densities. Lab on a chip. 7:987–994.

Mohammed JS, Caicedo HH, Fall CP, Eddington DT. 2008. Microfluidic add-on for standard electrophysiology chambers. Lab on a chip. 8:1048–1055.

Mountcastle VB. 1997. The columnar organization of the neocortex. Brain : a journal of neurology. 120 (Pt 4):701–722.

Myers R. 1967. Transfusion of cerebrospinal fluid and tissue bound chemical factors between the brains of conscious monkeys: a new neurobiological assay☆. Physiology & Behavior. 2:373–377.

Myllymaa S, Myllymaa K, Korhonen H, Töyräs J, Jääskeläinen JE, Djupsund K, Tanila H, Lappalainen R. 2009. Fabrication and testing of polyimide-based microelectrode arrays for cortical mapping of evoked potentials. Biosensors & bioelectronics. 24:3067–3072.

Neeves KB, Lo CT, Foley CP, Saltzman WM, Olbricht WL. 2006. Fabrication and characterization of microfluidic probes for convection enhanced drug delivery. Journal of controlled release : official journal of the Controlled Release Society. 111:252–262.

Nicholson C. 1993. Ion-selective microelectrodes and diffusion measurements as tools to explore the brain cell microenvironment. Journal of neuroscience methods. 48:199–213.

Nicholson C, Phillips JM. 1981. Ion diffusion modified by tortuosity and volume fraction in the extracellular microenvironment of the rat cerebellum. The Journal of physiology. 321:225–257.

Nicholson C, Tao L. 1993. Hindered diffusion of high molecular weight compounds in brain extracellular microenvironment measured with integrative optical imaging. Biophysical journal. 65:2277–2290.

Nimmerjahn A, Kirchhoff F, Kerr JND, Helmchen F. 2004. Sulforhodamine 101 as a specific marker of astroglia in the neocortex in vivo. Nature methods. 1:31–37.

Olesen J, Larsen B, Lauritzen M. 1981. Focal hyperemia followed by spreading oligemia and impaired activation of rCBF in classic migraine. Annals of neurology. 9:344–352.

Paik S-J, Park Y, Cho DD. 2003. Roughened polysilicon for low impedance microelectrodes in neural probes. Journal of Micromechanics and Microengineering. 13:373–379.

Passeraub PA, Almeida A, Thakor N. 2003. Design, microfabrication and analysis of a microfluidic chamber for the perfusion of brain tissue slices. Biomedical Microdevices. 5:147–155.

Pearce TM, Williams JJ, Kruzel SP, Gidden MJ, Williams JC. 2005. Dynamic control of extracellular environment in in vitro neural recording systems. IEEE transactions on neural systems and rehabilitation engineering : a publication of the IEEE Engineering in Medicine and Biology Society. 13:207–212.

Peterman MC. 2003. Localized Neurotransmitter Release for Use in a Prototype Retinal Interface. Investigative Ophthalmology & Visual Science. 44:3144–3149.

Peterman MC, Noolandi J, Blumenkranz MS, Fishman HA. 2004. Localized chemical release from an artificial synapse chip. Proceedings of the National Academy of Sciences of the United States of America. 101:9951–9954.

Pologruto TA, Sabatini BL, Svoboda K. 2003. ScanImage: flexible software for operating laser scanning microscopes. Biomedical engineering online. 2:13.

Purves D, Riddle DR, LaMantia AS. 1992. Iterated patterns of brain circuitry (or how the cortex gets its spots). Trends in neurosciences. 15:362–368.

Queval A, Ghattamaneni NR, Perrault CM, Gill R, Mirzaei M, McKinney RA, Juncker D. 2010. Chamber and microfluidic probe for microperfusion of organotypic brain slices. Lab on a chip. 10:326–334.

Rajaraman S, Choi S-O, Shafer RH, Ross JD, Vukasinovic J, Choi Y, DeWeerth SP, Glezer A, Allen MG, Bragg J a. 2007. Micromachined three-dimensional electrode arrays for

transcutaneous nerve tracking. Journal of Micromechanics and Microengineering. 17:085014.

Rambani K, Vukasinovic J, Glezer A, Potter SM. 2009. Culturing thick brain slices: an interstitial 3D microperfusion system for enhanced viability. Journal of neuroscience methods. 180:243–254.

Rodgers CI, Armstrong GAB, Shoemaker KL, LaBrie JD, Moyes CD, Robertson RM. 2007. Stress preconditioning of spreading depression in the locust CNS. PloS one. 2:e1366.

Russell MB, Olesen J. 1996. A nosographic analysis of the migraine aura in a general population. Brain. 119:355–361.

Rutten WLC. 2002. Selective electrical interfaces with the nervous system. Annual review of biomedical engineering. 4:407–452.

Sarje a, Thakor N. 2004. Neural interfacing. Conference proceedings : . Annual International Conference of the IEEE Engineering in Medicine and Biology Society IEEE Engineering in Medicine and Biology Society Conference. 7:5325–5328.

Schweitzer JS, Patrylo PR, Dudek FE. 1992. Prolonged field bursts in the dentate gyrus: dependence on low calcium, high potassium, and nonsynaptic mechanisms. J Neurophysiol. 68:2016–2025.

Scott A, Weir K, Easton C, Huynh W, Moody WJ, Folch A. 2012. A microfluidic microelectrode array for simultaneous electrophysiology, chemical stimulation, and imaging of brain slices. Lab on a chip.

Shiku H, Yamakawa T, Nashimoto Y, Takahashi Y, Torisawa Y-S, Yasukawa T, Ito-Sasaki T, Yokoo M, Abe H, Kambara H, Matsue T. 2009. A microfluidic dual capillary probe to collect messenger RNA from adherent cells and spheroids. Analytical biochemistry. 385:138–142.

Shinohara M, Dollinger B, Brown G, Rapoport S, Sokoloff L. 1979. Cerebral glucose utilization: local changes during and after recovery from spreading cortical depression. Science (New York, NY). 203:188–190.

Snow RW, Taylor CP, Dudek FE. 1983. Electrophysiological and optical changes in slices of rat hippocampus during spreading depression. Journal of neurophysiology. 50:561–572.

Somjen GG. 1979. Extracellular potassium in the mammalian central nervous system. Annual review of physiology. 41:159–177.

Somjen GG. 2001. Mechanisms of spreading depression and hypoxic spreading depression-like depolarization. Physiological reviews. 81:1065–1096.

Somjen GG, Rosenthal M, Cordingley G, LaManna J, Lothman E. 1976. Potassium, neuroglia, and oxidative metabolism in central gray matter. Federation proceedings. 35:1266–1271.

Stieglitz T. 2001. Flexible biomedical microdevices with double-sided electrode arrangements for neural applications. Sensors and Actuators A: Physical. 90:203–211.

Syková E, Nicholson C. 2008. Diffusion in Brain Extracellular Space. Physiol Rev. 88:1277–1340.

Takeuchi S, Ziegler D, Yoshida Y, Mabuchi K, Suzuki T. 2005. Parylene flexible neural probes integrated with microfluidic channels. Lab on a chip. 5:519–523.

Tang YT, Kim J, López-Valdés HE, Brennan KC, Ju YS. 2011. Development and characterization of a microfluidic chamber incorporating fluid ports with active suction for localized chemical stimulation of brain slices. Lab on a chip. 11:2247–2254.

Tao L. 2000. Light scattering in brain slices measured with a photon counting fiber optic system. Journal of Neuroscience Methods. 101:19–29.

Teyler TJ. 1980. Brain slice preparation: Hippocampus. Brain Research Bulletin. 5:391–403.

Thiébaud P, Beuret C, Koudelka-Hep M, Bove M, Martinoia S, Grattarola M, Jahnsen H, Rebaudo R, Balestrino M, Zimmer J, Dupont Y. 1999. An array of Pt-tip microelectrodes for extracellular monitoring of activity of brain slices. Biosensors & bioelectronics. 14:61–65.

Tsai PS, Kaufhold JP, Blinder P, Friedman B, Drew PJ, Karten HJ, Lyden PD, Kleinfeld D. 2009. Correlations of neuronal and microvascular densities in murine cortex revealed by direct

counting and colocalization of nuclei and vessels. The Journal of neuroscience : the official journal of the Society for Neuroscience. 29:14553–14570.

Van Harreveld A, Stamm JS. 1954. Consequences of cortical convulsive activity in rabbit. Journal of neurophysiology. 17:505–520.

Walz W. 2002. Chloride/anion channels in glial cell membranes. Glia. 40:1–10.

Welker C. 1976. Receptive fields of barrels in the somatosensory neocortex of the rat. The Journal of comparative neurology. 166:173–189.

Woods RP, Iacoboni M, Mazziotta JC. 1994. Bilateral spreading cerebral hypoperfusion during spontaneous migraine headache. The New England journal of medicine. 331:1689–1692.

Woolsey TA, Rovainen CM, Cox SB, Henegar MH, Liang GE, Liu D, Moskalenko YE, Sui J, Wei L. n.d. Neuronal units linked to microvascular modules in cerebral cortex: response elements for imaging the brain. Cerebral cortex (New York, NY : 1991). 6:647–660.

Xia Y, Whitesides GM. 1998. Soft Lithography. Angewandte Chemie International Edition. 37:550–575.

Yang M, Li C-W, Yang J. 2002. Cell Docking and On-Chip Monitoring of Cellular Reactions with a Controlled Concentration Gradient on a Microfluidic Device. Analytical Chemistry. 74:3991–4001.

Young W. 1980. Spreading depression in elasmobranch cerebellum. Brain Research. 199:113–126.

Zador Z, Magzoub M, Jin S, Manley GT, Papadopoulos MC, Verkman a S. 2008. Microfiberoptic fluorescence photobleaching reveals size-dependent macromolecule diffusion in extracellular space deep in brain. The FASEB journal : official publication of the Federation of American Societies for Experimental Biology. 22:870–879.